

---

# Disentangling Representations in RNNs through Multi-task Learning

---

**Pantelis Vafidis**

Computation & Neural Systems  
Caltech  
pvafeidi@caltech.edu

**Aman Bhargava**

Computation & Neural Systems  
Caltech  
abhargav@caltech.edu

**Antonio Rangel**

Humanities and Social Sciences  
Caltech  
arangel@caltech.edu

## Abstract

Abstract, or disentangled, representations are a promising mathematical framework for efficient and effective generalization in both biological and artificial systems. We investigate abstract representations in the context of multi-task classification over noisy evidence streams – a canonical decision-making neuroscience paradigm. We derive theoretical bounds that guarantee the emergence of disentangled representations in the latent state of any optimal multi-task classifier, when the number of tasks exceeds the dimensionality of the state space. We experimentally confirm that RNNs trained on multi-task classification learn disentangled representations in the form of continuous attractors, leading to zero-shot out-of-distribution (OOD) generalization. We demonstrate the flexibility of the abstract RNN representations across various decision boundary geometries and in tasks requiring classification confidence estimation. Our framework suggests a general principle for the formation of cognitive maps that organize knowledge to enable flexible generalization in biological and artificial systems alike, and closely relates to representations found in humans and animals during decision-making and spatial reasoning tasks.

## 1 Introduction

Humans and animals can generalize to new settings effortlessly, leveraging a combination of past experiences and world models [43, 44]. Modern foundation models also display emergent out-of-distribution (OOD) generalization abilities, in the form of zero- or few-shot learning [10, 59, 36, 57]. For generalization, it is crucial to have appropriate representations which extrapolate or interpolate previous experiences [67, 35, 38], or the use of task compositionality as an inductive bias [76, 62].

One mechanism for generalization is through abstract, or *disentangled*, representations [29, 39, 38]. A property of abstract representations is that they preserve the latent structure present in the world in their geometry, i.e. they are low-dimensional, rectangular, and compositional, each axis corresponding to a *factor of variation* in the data. Then a linear decoder (i.e. downstream neuron) trained to discriminate between two categories can readily generalize to stimuli not observed in training, due to the structure of the representation. From a neuroscience perspective, this corresponds to decomposing a novel stimulus into its familiar attributes, and reasoning based on those. For instance, imagine you are at a grocery store, deciding whether a fruit is ripe or not. If the brain’s internal representation of food attributes (ripeness, caloric content, etc.) is disentangled, then learning to perform this task for bananas would lead to zero-shot generalization to other fruit (e.g. mangos, Figure 1a).

This raises the question of under which conditions do such representations emerge in biological and artificial agents alike. Several brain areas including the amygdala, prefrontal cortex and hippocampus have been found to encode variables of interest in an abstract format [65, 5, 8, 55, 16]. Previous work showed that feedforward neural networks develop abstract representations when trained to multitask [38]. However, real-world decisions typically rely on imperfect, noisy information, evolving dynamically over time [9, 41]. To account for this important feature of the world, we train RNNs to multitask canonical neuroscience tasks involving the accumulation of evidence over noisy streams.

**Contributions.** The main contributions of this paper are the following:

- We prove that any optimal multi-task classifier is guaranteed to learn a disentangled representation of the ground truth contained in the noisy measurements in its latent state, if the classification boundary normal vectors span the input space (Appendix B). Intriguingly, noise in the observations is necessary to guarantee the latent state would compute an optimal, disentangled representation of the ground truth.
- Through experiments, we confirm that RNNs trained to multitask develop abstract representations that zero-shot generalize OOD, when the number of tasks exceeds the input dimensionality. The computational substrate of these representations is a 2D continuous attractor [2] storing a ground truth estimate in a product space of the latent factors.
- We demonstrate that our setting is robust to a number of manipulations, including interleaved learning of linear and non-linear tasks and free reaction time decisions.
- Finally, we discuss the relation between our results and important neuroscientific findings, their implications for generalizable representation learning in artificial systems, and demonstrate the strong advantage of multitasking over previously proposed mechanisms of representation learning in the brain [48, 76].

Despite being framed in the context of neuroscience, our results are general; they apply to any system aggregating noisy evidence over time.

## 1.1 Related work

Disentanglement has long been recognized as a promising strategy for generalization [4] (although note [46, 54] for a contrarian view), yet most modern work focuses on feedforward architectures [29, 39, 74]. In terms of autoregressive models, Hsu et al. [33], Li and Mandt [45] showed that variational LSTMs disentangle representations of underlying factors in sequential data allowing style transfer; however to the best of our knowledge the underlying representational geometry has not been characterised. Other work focuses on fitting RNNs to behavioral data while enforcing disentanglement for interpretability [18, 51]. Work on context-dependent decision making has shown that RNNs re-purpose learned representations in a compositional manner when trained in related tasks [76, 20]; however, the abstractness of the resulting representations was not established. Finally John et al. [37] show that multitasking results in disentanglement, however they directly enforce latent factor separation through their adversarial optimization objectives. Our approach is most closely related to weakly supervised disentanglement, without comparing across samples [66].

Previous work showed that multitasking feedforward networks learn abstract representations, as quantified by regression generalization [38]. We expand upon these findings in several ways. First, we extend the framework of Johnston and Fusi [38] to RNNs that can update their representations as further information arrives. Second, we prove theorems on optimal multi-task classifiers that guarantee the emergence of disentangled representations **in any optimal multitask classifier** if the number of tasks exceeds the input dimensionality  $D$ . Third, we rigorously analyze the role of noise in forming disentangled representations, extending the noise-free regime studied in [38]. Finally, we explore a range of values for  $D$ , providing experimental validation of our theory. Whereas related work proved that disentangled representations emerge in feedforward architectures from multitask learning in sparse tasks when a sparsity regularization constraint is placed on the predictors [42], we place no such constraints and still uncover disentangled representations.

## 2 Model and setup

### 2.1 Problem formulation

We consider canonical cognitive neuroscience tasks that involve evidence aggregation over time, mirroring decision-making under uncertainty. The input consists of  $D$  noisy evidence streams  $\mathbf{X}(t) \in \mathbb{R}^D$  where  $\mathbf{X}(t) = \mathbf{x}^* + \sigma \mathcal{N}(\mathbf{0}, \mathbf{I}_D)$  and  $\mathbf{x}^* \in \mathbb{R}^D$  is the ground truth evidence in a certain trial ( $x_i^* \sim \text{Uniform}(-0.5, 0.5)$ ) and  $\sigma$  is the input noise standard deviation (Figure 1c, left). Each element  $x_i^*$  of  $\mathbf{x}^*$  corresponds to different options under consideration or different attributes of the same item. The target output  $\mathbf{y}(\mathbf{x}^*) \in \{-1, +1\}^{N_{\text{task}}}$  is a vector of  $N_{\text{task}} + 1$ s and  $-1$ s, depending on whether  $\mathbf{x}^*$  is above or below each of the classification boundaries (Figure 1b). To ensure the reproducibility of our results, we incorporate our tasks within the NeuroGym framework [53].

The decision maker should integrate noisy samples  $\mathbf{X}(t)$  over time, viewed through an injective observation map (encoder)  $f$ , to estimate  $\hat{\mathbf{Y}}_i(t) = \Pr\{y_i(\mathbf{x}^*) = 1 | f(\mathbf{X}(1)), \dots, f(\mathbf{X}(t))\}$  (Figure S2). The classification lines reflect criteria based on which decisions will be made. Imagine for example that  $x_1$  corresponds to food and  $x_2$  to water reward. Depending on the agent’s internal state, one could take precedence over the other, and the degree of preference is reflected in the slope of the line. In Appendix B we prove that any optimal multi-task classifier will learn disentangled representations of  $\mathbf{x}^*$  in its latent state  $\mathbf{Z}(t)$ , when the  $N_{\text{task}}$  classification boundaries span the latent space.

### 2.2 Architecture

We train leaky RNNs which represent a brain area responsible for decision-making to multitask the aforementioned tasks. The networks contain  $N_{\text{neu}} = 64$  neurons, and their activations  $\mathbf{z}(t)$  obey:

$$\tau \frac{d\mathbf{z}(t)}{dt} = -\mathbf{z}(t) + [\mathbf{W}_{\text{rec}} \mathbf{z}(t) + \mathbf{W}_{\text{in}} \mathbf{x}_{\text{in}}(t) + \mathbf{b}]_+ \quad (1)$$

where  $\mathbf{W}_{\text{rec}}$  is the recurrent weight matrix,  $\mathbf{W}_{\text{in}}$  is the matrix carrying the input vector  $\mathbf{x}_{\text{in}}$ ,  $\mathbf{b}$  is a unit-specific bias vector,  $\tau$  is the neuronal time constant and  $[\cdot]_+$  is the ReLU applied element-wise to a vector. We simulate Equation (1) using the forward Euler method for  $T = 20$  timesteps of duration  $\Delta t = \tau = 100$  ms, which we find to be stable. The RNN’s output  $\hat{\mathbf{y}}(t)$  of size  $N_{\text{task}}$  is given by:

$$\hat{\mathbf{y}}(t) = g(\mathbf{W}_{\text{out}} \mathbf{z}(t)) \quad (2)$$

where  $\mathbf{W}_{\text{out}}$  is a readout matrix and  $g$  the output activation function applied elementwise. We choose  $g(z) = \tanh(z)$  for classification,  $5 \tanh(z)$  for integration-to-bound, and  $g(z) = z$  for other tasks. The inputs described above are first passed through a randomly initialized encoder  $f$ , which represents a static mapping from latents to observations (e.g. a perceptual system). The encoder is a 3-layer MLP with hidden dimensions 100, 100, 40 and ReLU non-linearities, is unique to each network and kept fixed during training. An additional fixation input which is 1 during the trial and turns 0 when the network should report its decisions is directly passed to the hidden layer (Figure 1c). The RNN is trained to produce the target outputs. By minimizing loss across trials, the network is incentivized to estimate  $\Pr\{y_i(\mathbf{x}^*) = +1\}$ . We use mean-squared-error loss and train all parameters (i.e.  $\mathbf{W}_{\text{rec}}$ ,  $\mathbf{W}_{\text{in}}$ ,  $\mathbf{W}_{\text{out}}$  and  $\mathbf{b}$ ) with Adam default settings except  $\text{lr} = 10^{-3}$  [40]. Table S1 summarizes all hyperparameters and their values. Network training takes  $\sim 10$  minutes on a commercial laptop CPU.

## 3 Theoretical Results

We seek to understand the properties of optimal multi-task classifiers with random variable latent state  $\mathbf{Z}(t)$  in the paradigm illustrated in Figure S2 and described in Section 2.1. Specifically, we are interested in classifiers that, at each time point  $t$ , estimate multiple linear classifications  $\mathbf{y}(\mathbf{x}^*) = [y_1(\mathbf{x}^*), \dots, y_{N_{\text{task}}}(\mathbf{x}^*)] \in \{0, 1\}^{N_{\text{task}}}$  based on noisy, potentially non-linearly mapped observations  $f(\mathbf{X}(1)), \dots, f(\mathbf{X}(t))$  with maximal likelihood. The classifier output at time  $t$ , denoted  $\hat{\mathbf{Y}}(t) \in [0, 1]^{N_{\text{task}}}$ , represents a set of Bernoulli random variable parameters, where each element  $\hat{Y}_i(t)$  corresponds to the probability  $\Pr\{y_i(\mathbf{x}^*) = 1 | f(\mathbf{X}(1)), \dots, f(\mathbf{X}(t))\}$ .

Each of the  $N_{\text{task}}$  decision boundaries can be expressed as a pair of boundary normal vector  $\mathbf{c}_i \in \mathbb{R}^D$  and offset  $b_i \in \mathbb{R}$  (Equation 8). Let  $\mathbf{C} \in \mathbb{R}^{N_{\text{task}} \times D}$  represent the matrix of decision boundaries and  $\mathbf{b} \in \mathbb{R}^{N_{\text{task}}}$  be the vector of decision boundary offsets.

**Theorem 3.1** (Disentangled Representation Theorem). *If  $\mathbf{C} \in \mathbb{R}^{N_{\text{task}} \times D}$  is a full-rank matrix and  $N_{\text{task}} \geq D$ , then*

1. *any optimal estimator of  $\mathbf{y}(\mathbf{x}^*)$  must encode an estimate  $\mu(t)$  of the ground truth evidence variable  $\mathbf{x}^*$  in its latent state  $\mathbf{Z}(t)$ , and*
2. *if the activation function  $g = \tanh$ ,  $\mu(t)$  will be **linearly decodable from  $\mathbf{Z}(t)$** , thus implying that  $\mathbf{Z}(t)$  contains a linear disentangled representation of  $\mu(t)$  [30, 38].*

Specifically,  $\mu(t)$  is the maximum likelihood estimate of  $\mathbf{x}^*$  given observations  $f(\mathbf{X}(1)), \dots, f(\mathbf{X}(t))$ . Equations 3, 4 are closed-form expressions for extracting  $\mu(t)$  from  $\mathbf{Z}(t)$  with a generic activation function  $g$  and  $g = \tanh$  respectively.

$$\mu(t) = (\mathbf{C}^\top \mathbf{C})^{-1} \mathbf{C}^\top \left( \frac{\sigma}{\sqrt{t}} \Phi^{-1}(g(\mathbf{Z}(t))) + \mathbf{b} \right) \quad (3)$$

$$\approx \underbrace{\frac{2\sqrt{3}\sigma}{\pi\sqrt{t}} (\mathbf{C}^\top \mathbf{C})^{-1} \mathbf{C}^\top \mathbf{Z}(t)}_{\text{Linear Function of } \mathbf{Z}(t)} + \underbrace{(\mathbf{C}^\top \mathbf{C})^{-1} \mathbf{C}^\top \mathbf{b}}_{\text{Affine Term}} \quad (4)$$

Where  $\Phi$  is the CDF of the normal distribution,  $\sigma$  is the noise magnitude and  $t$  the trial duration.

*Proof.* Point 1 and Equation 3 are proven in Appendix B in Theorem B.6. Point 2 and Equation 4 are proven in Corollary B.7.  $\square$

Theorem 3.1 holds for *any* system that performs optimal multi-task classification based on noisy, injectively transformed observations  $f(\mathbf{X}(t))$  (e.g., RNNs, biological neural circuits, Bayesian filters, etc.). Our results are readily extensible to sub-optimal multi-task classification models under the assumption that classification error w.r.t. optimal estimation is randomly distributed with zero mean (see Appendix B). In this case, the closed-form solutions in Equations 3, 4 correspond to a least-squared error estimate of  $\mu(t)$  given sub-optimal  $\mathbf{Z}(t)$ . Surprisingly, our theoretical results indicate  $\mathbf{Z}(t)$  will contain a disentangled representation of  $\mathbf{x}^*$  when the readout map  $g(\mathbf{Z}(t)) := \hat{\mathbf{Y}}(t)$  is a tanh function (Equation 4, Corollary B.7). Our theoretical framework readily generates testable predictions for our computational experiments, including theoretical  $r^2$  values for estimating  $\mathbf{x}^*$  from  $\mathbf{Z}(t)$  (Appendix A.3, Figure S9a), and decodability of  $\mathbf{x}^*$  from  $\mathbf{Z}(t)$  as a function of latent dimension  $D$  (Figure 3a), number of tasks  $N_{\text{task}}$  (Figure 1f,g, 2c), noise level  $\sigma$  (Figure 3b), evidence aggregation time  $t$  (Lemma B.3), and latent factor correlation (Figure S6).

## 4 Experiments

### 4.1 Multitasking leads to disentangled representations

We train RNNs to do simultaneous classifications for 24 linear partitions of the latent space for  $D = 2$  (Figure 1b, 6 partitions shown). Figure 1d shows the top 3 PCs (capturing  $\sim 85\%$  of the variance) of network activity after training (final accuracies  $\sim 95\%$ ) for multiple trials, along with the fixed points of network dynamics. To find the fixed points, we follow a standard procedure outlined in Sussillo and Barak [69] (see Appendix A.1 for details). Looking at Figure 1d the fixed points span the entire two-dimensional manifold that the trials evolve in, which corresponds to a continuous attractor with stable states across a 2D "sheet". This means that the network can store a short-term memory [73] of the current amount of accumulated evidence in a product space of the latent variables.

Furthermore, the representation is low-dimensional, rectangular and compositional; all characteristics of disentangled representations. In comparison, the representations after the encoder are non-linearly mixed, high-dimensional and overlapping (Figure S5a). Individual trials with noise show how the representation maintains a sense of metric distances in the RNN representation space (Figure S5b). Figure S5c demonstrates how this representation comes about during learning, and Figure S5d that

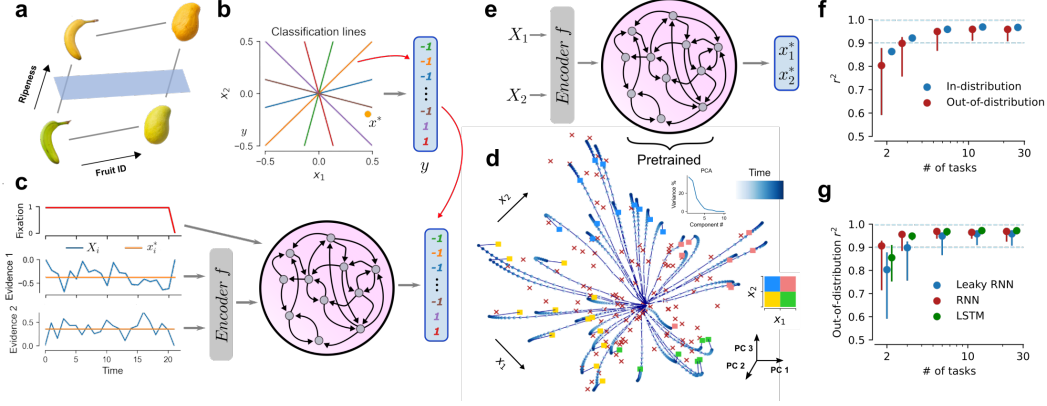


**Figure 1: Learning disentangled representations.** (a) A disentangled representation directly lends itself to OOD generalization: a downstream linear decoder can differentiate ripe from unripe bananas and can readily generalize to mangos, even though it has never been trained on mangos. (b) The task is to simultaneously report whether the ground truth  $\mathbf{x}^*$  lies above (+1) or below (−1) a number of classification lines. (c) RNNs are trained to report the outcome of all the binary classifications in b at the end of the trial (indicated by the fixation input turning 0). (d) Top 3 PCs of RNN activity. Each line is a trial, while color saturation indicates time. All trials start from the center and move outwards, towards the location of  $\mathbf{x}^*$  in state space. We color the last timepoint in each trial (squares) according to the quadrant this trial was drawn from. Red x's correspond to attractors (see Appendix A.1). Here we remove input noise so that trajectories can be visualized easier. The network learns a two-dimensional continuous attractor that seems to provide a disentangled representation of the state space. (e) To evaluate OOD generalization, we train a linear decoder (see a) to output the ground truth  $\mathbf{x}^*$  at the end of the trial, while keeping network weights frozen. (f) ID and OOD generalization performance for networks trained in different number of tasks  $N_{task}$ . We report the 25, 50 and 75 percentile of  $r^2$  for each network size (see Appendix A.2). ID and OOD performance increase with number of tasks, and the generalization gap decreases, indicating that the networks have indeed learned abstract representations. (g) The results hold for other recurrent architectures.

the short-term memory persists when a delay period is included before the decision. Therefore, it seems that multitasking has led to disentangled, persistent representations of the latent variables. Importantly, and in line with our theory, this only happens when noise is present in the input, which forces the network to learn a notion of distance from classification boundaries. Indeed, when the network is trained without input noise, it does not learn a 2D continuous attractor (Figure S5e).

To quantify the disentanglement of the representations, we evaluate regression generalization by training a linear decoder to predict the ground truth  $\mathbf{x}^*$  while network weights are frozen (Figure 1e). We perform out-of-distribution 4-fold crossvalidation, i.e. train the decoder on 3 out of 4 quadrants and test in the remaining quadrant (Appendix A.2 for details). We also evaluate in-distribution (ID) performance by training the decoder in all quadrants. An example of train and test losses is shown in Figure S5f. We find that the network's OOD and ID generalization performance are excellent (median  $r^2 = 0.96, 0.97$  respectively across 5 example networks, also see Figure 1f); therefore the network has indeed learned a disentangled representation that zero-shot generalizes OOD. In addition, ID performance increases with the number of tasks  $N_{task}$ , and the OOD generalization gap decreases (Figure 1f). Therefore we conclude that simultaneously training an RNN in classification tasks that span the latent space results in disentangled representations in the recurrent hidden layer.

Since  $\mathbf{x}^*$  can be decoded by this representation in unseen (by the decoder) parts of the state space, it follows that the representation can be used to solve **any** task involving the same underlying variables, without requiring further pretraining. In other words, to solve any other task we do not need to deal with the denoising and unmixing of the latent factors  $x_1, x_2$ ; we would just need to learn the (non-linear) mapping from  $x_1, x_2$  to task output. Crucially, these findings are architecture-agnostic: they hold for non-leaky ("vanilla") RNNs, which outperform leaky ones, and LSTMs which drastically reduce performance variability (Figure 1g). We still choose leaky RNNs because of their closer correspondence to biological neurons, which have a membrane voltage that decays over time.

We were also curious to see the impact of correlated inputs. A problem with high correlations is that they render parts of the state space virtually invisible to the network (Figure S6a). Surprisingly, OOD generalization performance is very weakly affected by input correlations, even though the state space is sampled uniformly in test (Figure S6b). The behavior is highly non-linear: performance is great until  $\rho = 0.97$ , but when the inputs are perfectly correlated ( $\rho = 1$ ), performance drop is sharp.

Finally, we examined RNN unit activations for these representations, and their relation to the latent variables. In Figure S7a we plot the steady-state firing rates for all 64 neurons, while regularly sampling  $x_1$  and  $x_2$ . Interestingly, we find that in these networks only  $\sim 10\%$  of neurons are active at any time, which is in line with sparse coding in the brain. In addition, the average firing rate is consistently  $\sim 0.25$  spikes/s, which is surprisingly close to cortical values. Furthermore, we find that all of the active neurons display mixed selectivity, i.e. they are tuned to both variables, which is a known property of cortical neurons [61] (Figure S7b). This suggests that metrics of disentanglement that assume that individual neurons encode distinct factors of variation [29, 39, 13, 32, 21] might be insufficient in detecting disentanglement in networks that generalize well. While recent work incorporates such axis-alignment in the definition of disentanglement, our work along with others [38] showcases the advantages of approaching disentanglement from a mixed representations perspective. Importantly, these properties were not imposed during training, nor was there any parameter fine tuning involved; rather they emerged from task structure and optimization objective.

## 4.2 Nonlinear tasks and interleaved learning

So far we have been training RNNs to perform linear classifications. However there are cases where the streams might need to be combined nonlinearly. For instance, if the two streams represent the amount and probability of reward respectively, an agent needs to multiply the two and decide whether the expected value exceeds a certain (metabolic) cost  $\gamma$  of performing an action to obtain said reward. Figure S8a shows the classification lines for the multiplicative task, where the network should decide whether the ground truth  $\mathbf{x}^*$  lies above or below the curve  $x_1 x_2 = \gamma$ , for multiple values of  $\gamma$ . RNNs trained on this task learn a representation that separates for trials in different quadrants (Figure S8b). This heuristic might have come about because individual classification lines span only a single quadrant for this task. Furthermore, trials belonging to the same quadrant seem to be more convoluted, with a corresponding drop in OOD performance (median  $r^2 = 0.71$ ), which might reflect the non-linearity of the task. Therefore, we wondered how the representation would look like if the network was trained on both the linear and multiplicative tasks, as animals need to do.

For that we perform interleaved training of both tasks (i.e. train in batches sampled from one of the tasks at a time), a setting where neural networks excel at, compared to humans who excel at blocked training, where tasks are learned sequentially (but see Flesch et al. [24]). Figure S8c shows that the network learns a two-dimensional continuous attractor, and the learned representation is no longer separated by quadrants. OOD generalization for this network is excellent, and almost identical to ID performance (median  $r^2 = 0.94, 0.97$  respectively). Overall, we conclude that our framework extends to interleaved learning of a mixture of linear and nonlinear tasks, which better reflects the challenges encountered by agents in the real world. Note that during interleaved training, linear and non-linear tasks are not performed simultaneously; yet they are in immediate succession which also places pressure to the network to gradually learn representations that satisfy all tasks. The relationship between interleaved learning and multitasking could be an interesting direction for future work.

## 4.3 Abstract representations are learned for a free reaction time, integrate to bound task

So far we have been training networks to produce a response at the end of the trial. However, in many situations agents are free to make a decision whenever they are certain enough. Therefore, we here seek to extend our framework to free reaction time (RT) decisions. A canonical model accounting for choices and reaction times in humans and animals is the drift-diffusion model [41, 11]. It is composed of an accumulator that integrates noisy evidence over time, until a certain amount of certainty, represented by a bound, is reached, triggering a decision. In the linear classification task setting, the accumulated amount of evidence at time  $t$  for a line with slope  $\alpha$ ,  $A_\alpha(t)$  is given by:

$$A_\alpha(t) = A_\alpha(t-1) + X_1(t) - \alpha X_2(t) \quad (5)$$

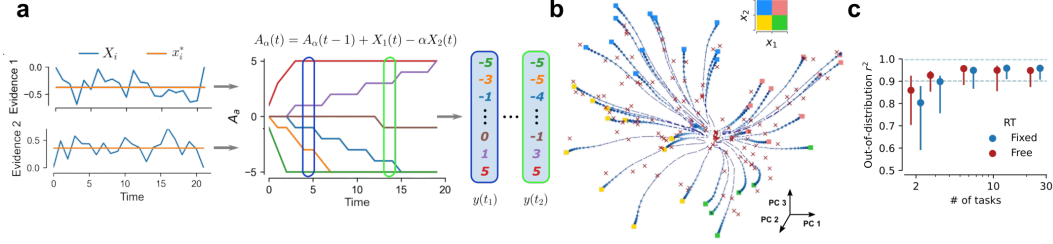


**Figure 2: Free reaction time task.** (a) Data generating process. Every classification line from Figure 1b now corresponds to an accumulator (see corresponding colors), and the desired output for the RNN is the accumulator values for the entire trial. The accumulator is quantized to integer values between  $\pm 5$ . (b) Representation for RNN trained on free reaction time task. The network learns a two-dimensional continuous attractor, similar to Figure 1d. (c) OOD generalization performance for the free reaction time (RT) task. Free RT outperforms fixed RT for a small number of tasks.

Intuitively,  $A_\alpha(t)$  reflects the amount of confidence at time  $t$  that the ground truth  $\mathbf{x}^*$  lies above or below the classification line with slope  $\alpha$ . Essentially, the network has to explicitly report distance from the classification lines, not just in which side of the line  $\mathbf{x}^*$  lies for that trial. We arbitrarily set the decision bound to  $\pm 5$ , and plot the accumulators  $A_\alpha$  for all lines in Figure 2a. Note that once the bound is reached a decision is effectively made and  $A_\alpha$  is kept constant. Also, instead of using continuous values, we quantize  $A_\alpha$ , because it is going to be used as target signal to train the network, and we do not want to introduce a strong inductive bias towards integrating the evidence streams.

We then train the RNN to reproduce confidence estimates from Figure 2a for the entire trial. Compared to previous experiments, the fixation input is no longer available to determine when to produce a decision. Instead, decisions evolve dynamically throughout the trial. Figure 2b shows that in this setting the network still learns a two-dimensional continuous attractor of the latent space. Furthermore, the free RT outperforms the fixed RT network (Figure 2c) for a small number of tasks, since it is explicitly required to report distance from the classification lines. However, as our theory shows (Lemma B.3) the fixed RT network is also implicitly reporting distance from the boundaries, when behaving like an optimal multi-task classifier, which explains the similar performance for a larger number of tasks. Overall, we showed that our setting accounts for naturalistic free RT decisions, and provides theoretical justification for the importance of confidence signals in the brain [64, 49].

#### 4.4 RNNs confirm and extend theoretical predictions

Here we explore the relation between the theory in Section 3 and Appendix B and experiments in Section 4 in more depth. First, we wondered why performance saturates in our networks to a high yet non-1  $r^2$ . The central limit theorem predicts that the estimate of the ground truth  $\mathbf{x}^*$  in any optimal multi-task classifier becomes more accurate with  $\sqrt{t}$ , providing a theoretical maximum  $r^2$  given trial duration  $T$  (Appendix A.3). Since the networks trained on the free RT task are required to output their confidence at any time in the trial, we can compute OOD  $r^2$  of network predictions at any timepoint  $t$ , and compare that to the theoretical prediction. Figure S9a shows that indeed the highest RNN  $r^2$  falls in the vicinity of or just short of the theoretical maximum. This indicates that RNNs trained with BPTT on these tasks behave like near-optimal multi-task classifiers that create increasingly accurate predictions with time, tightening the relation between our theoretical and experimental results.

An important prediction of our theory is that to learn abstract representations  $N_{task}$  should exceed  $D$ . To test this, we increase  $D$  (adding more inputs to Figure 1c), and vary  $N_{task}$ . Sampling classification hyperplanes methodically in high-dimensional spaces is non-trivial; therefore we resort to randomly sampling them. Figure 3a shows OOD generalization performance for various combinations of  $D$  and  $N_{task}$ . We observe that performance is bad when the  $N_{task} < D$ , but it increases when  $N_{task} \geq D$ . This increase is abrupt for smaller  $D$  and more gradual for higher, which is in line with remarks by Johnston and Fusi [38] that it is easier to learn abstract representations when  $D$  is high. Overall, our findings confirm our theory that abstract representations emerge when  $N_{task} \geq D$ . This result is remarkable, especially for high  $D$ , because it goes against our intuition that  $N_{task}$  should scale exponentially with  $D$  to fill up the space adequately; instead it need only scale linearly.

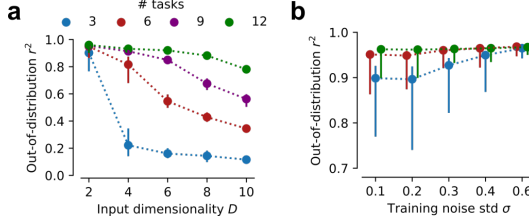


Figure 3: **RNNs confirm theoretical predictions.** (a) OOD  $r^2$  as a function of input dimensionality  $D$  and number of tasks  $N_{task}$ . Good values of  $r^2$  are obtained when  $N_{task} \geq D$ , confirming our theoretical results. (b) Increasing amounts of noise in pretraining results in better OOD generalization.

pretraining, while testing with the same  $\sigma = 0.2$ . Indeed, increasing amounts of noise consistently result in better OOD generalization (Figure 3b). This benefit comes for smaller numbers of tasks, allowing us to consider less supervised tasks (e.g. 3), train on them with more noise, and achieve the same performance as more tasks (e.g. 12). So even though networks with more noise perform worse in pretraining (low 90% classification accuracy), they learn more disentangled representations. These findings are highly non-trivial, and have informed our thinking about generalization and inherent variability of the underlying latent factors.

Finally, we were curious to see what happens if part of the state space was not crossed by task boundaries. To test this, we train a network for  $D = 2$  on classification tasks that only tile quadrants 1 and 3 (Figure S9b). Note that trials are still drawn from the entire state space – however the network need not differentiate between points drawn within quadrant 2 or 4. The network still learns a two-dimensional continuous attractor; however the representation is no longer disentangled, likely because the boundaries are far away if  $\mathbf{x}^*$  is in quadrants 2 or 4 (Figure S9c). A more entangled representation may lead to poorer generalization performance, as measured by OOD regression generalization [38]. Indeed, we find that OOD performance of the tangled network is considerably worse (median  $r^2 = 0.80$ ), and most importantly it performs badly in the quadrants that are not spanned by classification lines (25 percentile  $r^2 = 0.62$ ). Therefore, it appears that in order to prevent the representations from tangling, tasks boundaries need to be distributed over the state space – as previously shown randomly sampling these boundaries is adequate.

## 5 Discussion

### 5.1 Implications for deep learning

Our work provides insight for understanding how and why “understanding” emerges from solving certain prediction tasks, which is particularly relevant to the study of foundation models [10, 31, 6]. Foundation models exhibit “understanding” of the world through semantically rich abstract representations that enable efficient downstream prediction. Our work suggests a profound connection between multi-task prediction and implicit knowledge of the underlying data generation process.

Consider an analogy with masked autoencoder vision foundation models, where  $\mathbf{x}^*$  is the “ground truth” of a scene (objects, positions, states, and relationships), the measurement variable  $\mathbf{X}$  is an image with missing patches [19, 28], and the model predicts the missing patch data  $y(\mathbf{x}^*)$ . The model’s latent variable  $\mathbf{Z}$  exhibits some “understanding” of  $\mathbf{x}^*$  in the form of abstract representations useful for downstream tasks. This analogy extends to masked language models [17] and autoregressive language models [60], where  $\mathbf{x}^*$  is “meaning” in a semantic space,  $\mathbf{X}(t)$  are words, and  $y$  is the next word. Localizing  $\mathbf{x}^*$  from  $\mathbf{Z}(t)$  relates to constructing a world model, showing that  $\mathbf{Z}$  represents  $\mathbf{x}^*$  abstractly and with high fidelity.

Our work provides a geometric starting point for understanding the correspondence between  $\mathbf{x}^*$  and  $\mathbf{Z}(t)$  in terms of mutual information  $I(\mathbf{x}^*; \mathbf{Z}(t))$  under various prediction tasks  $y(\mathbf{x}^*)$ . Relating the properties of prediction task  $y$  with  $\mathbf{x}^*$  and  $\mathbf{Z}(t)$  has implications for optimal synthetic data generation

Our theory and experiments provide insight on the importance of noise for developing efficient, abstract representations (Figure S5e). The closer to a classification boundary the ground truth  $\mathbf{x}^*$  is, the more likely noise will cross over the boundary. Since, as our theory shows, any optimal multi-task classifier has to estimate  $\Pr\{y_i(\mathbf{x}^*) = +1\}$ , and said probability directly relates to the actual distance from the boundary, it follows that noise allows the model to learn distances from boundaries, leading to efficient localization. We reasoned that additional noise might be even more beneficial, as it would allow more accurate estimation of  $\Pr\{y_i(\mathbf{x}^*) = +1\}$ , especially when  $\mathbf{x}^*$  is far from the boundary. To test this, we increase noise strength  $\sigma$  during



and novel unsupervised learning objectives for foundation models. The formulation is fundamental, with clear informational and geometric constructions amenable to both theory and experiment.

We demonstrated that even simple binary multi-task classification forces an optimal estimator of  $\mathbf{x}^*$  in  $\mathbf{Z}(t)$ . Binary classification is a low information objective, as it only requires the model to predict  $N_{task}$  bits that are deterministic functions of a continuous  $D$ -dimensional vector  $\mathbf{x}^*$ . The fact that an optimal estimator can be recovered under such conditions (i.e.,  $H(\mathbf{x}^*) \gg H(y_1, \dots, y_{N_{task}})$ ) is remarkable. Higher resolution prediction targets may yield the same or better estimation of  $\mathbf{x}^*$ , yet we already proved that the multi-task binary case achieves optimal estimation. Therefore, predicting masked out parts of an image during self-supervised learning or next word prediction in LLMs, which are richer objectives, should perform at least as well as our experiments. In fact, evidence for the latter already exist at the form of abstract, monosemantic concepts in LLMs [70].

Finally, the present work emphasizes the importance of the diversity and quality of data, rather than quantity, for generalization (an argument also made by Arora and Goyal [3]). Indeed, our experiments show that few uniformly spaced classification boundaries outperform many that over-sample part of the state space, ignoring others (Figure 1f, Figure S9b,c). Thus, we hope that this work will serve as inspiration for developing efficient and generalizable deep learning systems.

## 5.2 Implications for neuroscience

An ongoing debate in the brain sciences is whether to solve tasks the brain learns abstracts representations, or simple input-to-output mappings. Here we show that training RNNs to multitask results in shared, disentangled representations of the latent variables, in the form of continuous attractors. In this multitask setting, one task acts as a regularizer for the others, by not letting the representation collapse, or overfit, to specific tasks [77]. In the brain, such pressure from multiple tasks could be imposed by thalamocortical loops for internal state-dependent action selection operating in parallel, while the integration occurs in corticostriatal circuits [63]. This framework is also consistent with proposed theories of parallel processing in cortical columns [27].

Our findings directly link to two important neuroscientific findings: spatial cognition and value-based decision-making. First, the tasks here bear close resemblance to path-integration, i.e. the ability of animals to navigate space only relying on their proprioceptive sense of linear and angular velocity [52, 12, 72]. In path-integration animals integrate velocity signals to get location, while here we integrate noisy evidence to get rid of the noise. We learn abstract representations in the form of a 2D "sheet" continuous attractor, while the computational substrate for path integration is a 2D toroidal attractor [25, 68] – not an abstract representation. The conditions under which a 2D sheet vs. toroidal continuous attractor is learned is a potential area of future research. Second, decision making experiments in monkeys result in a 2D abstract representation in the medial frontal cortex, which supports novel inferential decisions [7]. Likewise, context-dependent decision-making experiments in humans also resulted in orthogonal, abstract representations [24].

The workhorse model for computational neuroscience has been context-dependent computation, where tasks are carried out one at a time and task identity is cued to the RNN by a one-hot vector [48]. However, this approach can be algorithmically inefficient, scaling linearly with the number of tasks, and exponentially with input dimensionality  $D$ . That is because context-dependent computation utilizes different parts of the state space for different tasks, and the resulting representations collapse to what is minimally required for each task (see [48, 75] and Appendix A.4). This can be detrimental for brains, which need to pack a lot of computation within a large yet limited neural substrate. In contrast, abstract representations are general, compact [47], can be used for **any** downstream task involving the same variables, scale linearly with  $D$ , and readily emerge from relatively simple tasks.

Overall, we believe that multitasking may present a paradigm shift for generalizable representation learning in biological and artificial systems alike. That is not to say that context-dependent representations are not useful; they are great at leveraging the compositional structure of tasks [76, 20], but tend to overfit to the specifics of the task, while multitask representations serve as world models applicable to various scenarios. Both types of representations are likely to be found in the brain.

### 5.3 Limitations

A limitation of the present work is that factorization is assumed. Yet not all problems are factorizable, or should be factorized. For instance, a more coarse-grained understanding of the world, that doesn't disentangle all factors, might be more suitable in many cases, and that might be reflected in the nature of the tasks. Furthermore, we focus on canonical cognitive neuroscience tasks which are somewhat removed from standard ML benchmarks. Normally, disentanglement methods would be tested against a benchmark such as dSprites [50]; however to the best of our knowledge no such benchmark exists for dynamic tasks where evidence has to be aggregated over time. Future work could endeavor to apply our setting to ML tasks, like self-supervised image completion, and showcase the potential benefits of scaling up the number of masked out pixels in relation to the dimensionality of the latent space  $D$ . Furthermore, we assume that noise is Gaussian and IID, which might not be always the case; yet our theory accounts for other noise distributions as long as the posterior  $P(\mathbf{x}^*|\mathbf{X}(1), \dots, \mathbf{X}(t))$  is non-zero everywhere and has a self-consistent/invariant maximum likelihood estimate over  $\mathbf{x}^*$  (see Appendix B).

### 5.4 Conclusion

We focus on the problem of optimal estimation of a latent ground truth  $\mathbf{x}^*$  from noisy, non-linear, high-dimensional versions of it. We provide theoretical guarantees that estimation succeeds when the amount of partial information about the truth available  $N_{task}$  scales linearly with the dimensionality of the latent space  $D$ . Our results hold for any injective mapping of latent variables to observables, which incorporates a vast range of transformations. They offer exciting implications for the manifold hypothesis [22], proving that the latent representations of optimal evidence aggregators observing high-dimensional world data inevitably estimate the structure of the low-dimensional manifold. Of particular interest is extending the theory to non-injective and non-deterministic observation maps  $f$ .

These findings shed light in the conditions under which biological and artificial systems alike develop representations that generalize well: they do so when there is enough pressure from many tasks that involve the same latent variables. Quoting Bengio et al. [4]: '... the most robust approach to feature learning is to *disentangle as many factors as possible, discarding as little information about the data as is practical*'. Apart from understanding learning in brains, we hope this work will inspire the development of deep learning systems with OOD generalization in mind.

### Acknowledgments and Disclosure of Funding

PV would like to thank the Onassis Foundation and AR the NOMIS Foundation for funding. AB thanks the NIH PTQN program for funding. No competing interests to declare. We would like to thank Yisong Yue and Stefano Fusi for early discussions, and Aiden Rosebush for early discussions of proof methods.

### References

- [1] Abdullahi Ali, Nasir Ahmad, Elgar de Groot, Marcel Antonius Johannes van Gerven, and Tim Christian Kietzmann. Predictive coding is a consequence of energy efficiency in recurrent neural networks. *Patterns*, 3(12):100639, December 2022. ISSN 2666-3899. doi: 10.1016/j.patter.2022.100639. URL <http://dx.doi.org/10.1016/j.patter.2022.100639>.
- [2] S Amari. Dynamics of pattern formation in lateral-inhibition type neural fields. *Biological Cybernetics*, 27(2):77–87, 1977. doi: 10.1007/bf00337259. URL <https://doi.org/10.1007/bf00337259>.
- [3] Sanjeev Arora and Anirudh Goyal. A theory for emergence of complex skills in language models, 2023. URL <https://arxiv.org/abs/2307.15936>.
- [4] Yoshua Bengio, Aaron Courville, and Pascal Vincent. Representation learning: A review and new perspectives, 2012. URL <https://arxiv.org/abs/1206.5538>.
- [5] Silvia Bernardi, Marcus K. Benna, Mattia Rigotti, Jérôme Munuera, Stefano Fusi, and C. Daniel Salzman. The geometry of abstraction in the hippocampus and prefrontal cortex. *Cell*, 183(4):

954–967.e21, November 2020. doi: 10.1016/j.cell.2020.09.031. URL <https://doi.org/10.1016/j.cell.2020.09.031>.

- [6] Rishi Bommasani, Drew A. Hudson, Ehsan Adeli, Russ Altman, Simran Arora, Sydney von Arx, Michael S. Bernstein, Jeannette Bohg, Antoine Bosselut, Emma Brunskill, Erik Brynjolfsson, Shyamal Buch, Dallas Card, Rodrigo Castellon, Niladri Chatterji, Annie Chen, Kathleen Creel, Jared Quincy Davis, Dora Demszky, Chris Donahue, Moussa Doumbouya, Esin Durmus, Stefano Ermon, John Etchemendy, Kawin Ethayarajh, Li Fei-Fei, Chelsea Finn, Trevor Gale, Lauren Gillespie, Karan Goel, Noah Goodman, Shelby Grossman, Neel Guha, Tatsunori Hashimoto, Peter Henderson, John Hewitt, Daniel E. Ho, Jenny Hong, Kyle Hsu, Jing Huang, Thomas Icard, Saahil Jain, Dan Jurafsky, Pratyusha Kalluri, Siddharth Karamcheti, Geoff Keeling, Fereshte Khani, Omar Khattab, Pang Wei Koh, Mark Krass, Ranjay Krishna, Rohith Kuditipudi, Ananya Kumar, Faisal Ladhak, Mina Lee, Tony Lee, Jure Leskovec, Isabelle Levent, Xiang Lisa Li, Xuechen Li, Tengyu Ma, Ali Malik, Christopher D. Manning, Suvir Mirchandani, Eric Mitchell, Zanele Munyikwa, Suraj Nair, Avanika Narayan, Deepak Narayanan, Ben Newman, Allen Nie, Juan Carlos Niebles, Hamed Nilforoshan, Julian Nyarko, Giray Ogut, Laurel Orr, Isabel Papadimitriou, Joon Sung Park, Chris Piech, Eva Portelance, Christopher Potts, Aditi Raghunathan, Rob Reich, Hongyu Ren, Frieda Rong, Yusuf Roohani, Camilo Ruiz, Jack Ryan, Christopher Ré, Dorsa Sadigh, Shiori Sagawa, Keshav Santhanam, Andy Shih, Krishnan Srinivasan, Alex Tamkin, Rohan Taori, Armin W. Thomas, Florian Tramèr, Rose E. Wang, William Wang, Bohan Wu, Jiajun Wu, Yuhuai Wu, Sang Michael Xie, Michihiro Yasunaga, Jiaxuan You, Matei Zaharia, Michael Zhang, Tianyi Zhang, Xikun Zhang, Yuhui Zhang, Lucia Zheng, Kaitlyn Zhou, and Percy Liang. On the opportunities and risks of foundation models, 2021. URL <https://arxiv.org/abs/2108.07258>.
- [7] A. Bongioanni, D. Folloni, L. Verhagen, J. Sallet, M. C. Klein-Flügge, and M. F. S. Rushworth. Activation and disruption of a neural mechanism for novel choice in monkeys. *Nature*, 591(7849):270–274, January 2021. doi: 10.1038/s41586-020-03115-5. URL <https://doi.org/10.1038/s41586-020-03115-5>.
- [8] Lara M. Boyle, Lorenzo Posani, Sarah Irfan, Steven A. Siegelbaum, and Stefano Fusi. Tuned geometries of hippocampal representations meet the demands of social memory, January 2022. URL <https://doi.org/10.1101/2022.01.24.477361>.
- [9] KH Britten, MN Shadlen, WT Newsome, and JA Movshon. The analysis of visual motion: a comparison of neuronal and psychophysical performance. *The Journal of Neuroscience*, 12(12):4745–4765, December 1992. doi: 10.1523/jneurosci.12-12-04745.1992. URL <https://doi.org/10.1523/jneurosci.12-12-04745.1992>.
- [10] Tom B. Brown, Benjamin Mann, Nick Ryder, Melanie Subbiah, Jared Kaplan, Prafulla Dhariwal, Arvind Neelakantan, Pranav Shyam, Girish Sastry, Amanda Askell, Sandhini Agarwal, Ariel Herbert-Voss, Gretchen Krueger, Tom Henighan, Rewon Child, Aditya Ramesh, Daniel M. Ziegler, Jeffrey Wu, Clemens Winter, Christopher Hesse, Mark Chen, Eric Sigler, Mateusz Litwin, Scott Gray, Benjamin Chess, Jack Clark, Christopher Berner, Sam McCandlish, Alec Radford, Ilya Sutskever, and Dario Amodei. Language models are few-shot learners, 2020. URL <https://arxiv.org/abs/2005.14165>.
- [11] Bingni W. Brunton, Matthew M. Botvinick, and Carlos D. Brody. Rats and humans can optimally accumulate evidence for decision-making. *Science*, 340(6128):95–98, April 2013. doi: 10.1126/science.1233912. URL <https://doi.org/10.1126/science.1233912>.
- [12] Yoram Burak and Ila R. Fiete. Accurate path integration in continuous attractor network models of grid cells. *PLoS Computational Biology*, 5(2):e1000291, February 2009. doi: 10.1371/journal.pcbi.1000291. URL <https://doi.org/10.1371/journal.pcbi.1000291>.
- [13] Tian Qi Chen, Xuechen Li, Roger B. Grosse, and David Duvenaud. Isolating sources of disentanglement in variational autoencoders. *CoRR*, abs/1802.04942, 2018. URL <http://arxiv.org/abs/1802.04942>.
- [14] Amit Choudhury. A simple approximation to the area under standard normal curve. *Mathematics and Statistics*, 2(3):147–149, 2014.

- [15] Olah Chris. Neural networks, manifolds, and topology – colah’s blog, April 2014. URL <https://colah.github.io/posts/2014-03-NN-Manifolds-Topology/>.
- [16] Hristos S Courellis, Juri Mixha, Araceli R Cardenas, Daniel Kimmel, Chrystal M Reed, Taufik A Valiante, C Daniel Salzman, Adam N Mamelak, Stefano Fusi, and Ueli Rutishauser. Abstract representations emerge in human hippocampal neurons during inference behavior. *bioRxiv*, pages 2023–11, 2023.
- [17] Jacob Devlin, Ming-Wei Chang, Kenton Lee, and Kristina Toutanova. BERT: pre-training of deep bidirectional transformers for language understanding. *CoRR*, abs/1810.04805, 2018. URL <http://arxiv.org/abs/1810.04805>.
- [18] Amir Dezfouli, Hassan Ashtiani, Omar Ghattas, Richard Nock, Peter Dayan, and Cheng Soon Ong. Disentangled behavioural representations. *Advances in neural information processing systems*, 32, 2019.
- [19] Alexey Dosovitskiy, Lucas Beyer, Alexander Kolesnikov, Dirk Weissenborn, Xiaohua Zhai, Thomas Unterthiner, Mostafa Dehghani, Matthias Minderer, Georg Heigold, Sylvain Gelly, Jakob Uszkoreit, and Neil Houlsby. An image is worth 16x16 words: Transformers for image recognition at scale, 2020. URL <https://arxiv.org/abs/2010.11929>.
- [20] Laura Driscoll, Krishna Shenoy, and David Sussillo. Flexible multitask computation in recurrent networks utilizes shared dynamical motifs. *bioRxiv*, pages 2022–08, 2022.
- [21] Cian Eastwood, Andrei Liviu Nicolicioiu, Julius von Kügelgen, Armin Kekić, Frederik Träuble, Andrea Dittadi, and Bernhard Schölkopf. Dci-es: An extended disentanglement framework with connections to identifiability, 2022. URL <https://arxiv.org/abs/2210.00364>.
- [22] Charles Fefferman, Sanjoy Mitter, and Hariharan Narayanan. Testing the manifold hypothesis, 2013. URL <https://arxiv.org/abs/1310.0425>.
- [23] Charles Fefferman, Sanjoy Mitter, and Hariharan Narayanan. Testing the manifold hypothesis. *Journal of the American Mathematical Society*, 29(4):983–1049, 2016.
- [24] Timo Flesch, David G. Nagy, Andrew Saxe, and Christopher Summerfield. Modelling continual learning in humans with hebbian context gating and exponentially decaying task signals, 2022. URL <https://arxiv.org/abs/2203.11560>.
- [25] Richard J. Gardner, Erik Hermansen, Marius Pachitariu, Yoram Burak, Nils A. Baas, Benjamin A. Dunn, May-Britt Moser, and Edvard I. Moser. Toroidal topology of population activity in grid cells. *Nature*, 602(7895):123–128, January 2022. doi: 10.1038/s41586-021-04268-7. URL <https://doi.org/10.1038/s41586-021-04268-7>.
- [26] James Gornet and Matthew Thomson. Automated mapping of virtual environments with visual predictive coding. *arXiv preprint arXiv:2308.10913*, 2023.
- [27] Jeff Hawkins, Marcus Lewis, Mirko Klukas, Scott Purdy, and Subutai Ahmad. A framework for intelligence and cortical function based on grid cells in the neocortex. *Frontiers in Neural Circuits*, 12, January 2019. ISSN 1662-5110. doi: 10.3389/fncir.2018.00121. URL <http://dx.doi.org/10.3389/fncir.2018.00121>.
- [28] Kaiming He, Xinlei Chen, Saining Xie, Yanghao Li, Piotr Dollár, and Ross Girshick. Masked autoencoders are scalable vision learners, 2021.
- [29] Irina Higgins, Loic Matthey, Arka Pal, Christopher Burgess, Xavier Glorot, Matthew Botvinick, Shakir Mohamed, and Alexander Lerchner. beta-VAE: Learning basic visual concepts with a constrained variational framework. In *International Conference on Learning Representations*, 2017. URL <https://openreview.net/forum?id=Sy2fzU9gl>.
- [30] Irina Higgins, David Amos, David Pfau, Sebastien Racaniere, Loic Matthey, Danilo Rezende, and Alexander Lerchner. Towards a definition of disentangled representations, 2018. URL <https://arxiv.org/abs/1812.02230>.

- [31] Jonathan Ho, Ajay Jain, and Pieter Abbeel. Denoising diffusion probabilistic models, 2020. URL <https://arxiv.org/abs/2006.11239>.
- [32] Kyle Hsu, Will Dorrell, James C. R. Whittington, Jiajun Wu, and Chelsea Finn. Disentanglement via latent quantization, 2023. URL <https://arxiv.org/abs/2305.18378>.
- [33] Wei-Ning Hsu, Yu Zhang, and James Glass. Unsupervised learning of disentangled and interpretable representations from sequential data, 2017. URL <https://arxiv.org/abs/1709.07902>.
- [34] Minyoung Huh, Brian Cheung, Tongzhou Wang, and Phillip Isola. The platonic representation hypothesis. *arXiv preprint arXiv:2405.07987*, 2024.
- [35] Takuya Ito, Tim Klinger, Douglas H. Schultz, John D. Murray, Michael W. Cole, and Mattia Rigotti. Compositional generalization through abstract representations in human and artificial neural networks, 2022. URL <https://arxiv.org/abs/2209.07431>.
- [36] Chao Jia, Yinfei Yang, Ye Xia, Yi-Ting Chen, Zarana Parekh, Hieu Pham, Quoc V. Le, Yunhsuan Sung, Zhen Li, and Tom Duerig. Scaling up visual and vision-language representation learning with noisy text supervision, 2021. URL <https://arxiv.org/abs/2102.05918>.
- [37] Vineet John, Lili Mou, Hareesh Bahuleyan, and Olga Vechtomova. Disentangled representation learning for non-parallel text style transfer, 2018. URL <https://arxiv.org/abs/1808.04339>.
- [38] W. Jeffrey Johnston and Stefano Fusi. Abstract representations emerge naturally in neural networks trained to perform multiple tasks. *Nature Communications*, 14(1), February 2023. doi: 10.1038/s41467-023-36583-0. URL <https://doi.org/10.1038/s41467-023-36583-0>.
- [39] Hyunjik Kim and Andriy Mnih. Disentangling by factorising. In Jennifer Dy and Andreas Krause, editors, *Proceedings of the 35th International Conference on Machine Learning*, volume 80 of *Proceedings of Machine Learning Research*, pages 2649–2658. PMLR, 10–15 Jul 2018. URL <https://proceedings.mlr.press/v80/kim18b.html>.
- [40] Diederik Kingma and Jimmy Ba. Adam: A method for stochastic optimization. *International Conference on Learning Representations*, 12 2014.
- [41] I. Krajbich, C. Armel, and A. Rangel. Visual fixations and the computation and comparison of value in simple choice. *Nature Neuroscience*, 13(10):1292–1298, 2010. doi: 10.1038/nn.2635. URL <https://doi.org/10.1038/nn.2635>.
- [42] Sebastien Lachapelle, Tristan Deleu, Divyat Mahajan, Ioannis Mitliagkas, Yoshua Bengio, Simon Lacoste-Julien, and Quentin Bertrand. Synergies between disentanglement and sparsity: Generalization and identifiability in multi-task learning. In Andreas Krause, Emma Brunskill, Kyunghyun Cho, Barbara Engelhardt, Sivan Sabato, and Jonathan Scarlett, editors, *Proceedings of the 40th International Conference on Machine Learning*, volume 202 of *Proceedings of Machine Learning Research*, pages 18171–18206. PMLR, 23–29 Jul 2023. URL <https://proceedings.mlr.press/v202/lachapelle23a.html>.
- [43] B. M. Lake, R. Salakhutdinov, and J. B. Tenenbaum. Human-level concept learning through probabilistic program induction. *Science*, 350(6266):1332–1338, December 2015. doi: 10.1126/science.aab3050. URL <https://doi.org/10.1126/science.aab3050>.
- [44] Brenden M. Lake, Tomer D. Ullman, Joshua B. Tenenbaum, and Samuel J. Gershman. Building machines that learn and think like people. *Behavioral and Brain Sciences*, 40, November 2016. doi: 10.1017/s0140525x16001837. URL <https://doi.org/10.1017/s0140525x16001837>.
- [45] Yingzhen Li and Stephan Mandt. Disentangled sequential autoencoder, 2018. URL <https://arxiv.org/abs/1803.02991>.

- [46] Francesco Locatello, Stefan Bauer, Mario Lučić, Gunnar Rätsch, Sylvain Gelly, Bernhard Schölkopf, and Olivier Frederic Bachem. Challenging common assumptions in the unsupervised learning of disentangled representations. In *International Conference on Machine Learning*, 2019. URL <http://proceedings.mlr.press/v97/locatello19a.html>. Best Paper Award.
- [47] Yi Ma, Doris Tsao, and Heung-Yeung Shum. On the principles of parsimony and self-consistency for the emergence of intelligence, 2022. URL <https://arxiv.org/abs/2207.04630>.
- [48] V. Mante, D. Sussillo, K. V. Shenoy, and W. T. Newsome. Context-dependent computation by recurrent dynamics in prefrontal cortex. *Nature*, 503(7474):78–84, November 2013. doi: 10.1038/nature12742. URL <https://doi.org/10.1038/nature12742>.
- [49] Paul Masset, Torben Ott, Armin Lak, Junya Hirokawa, and Adam Kepecs. Behavior- and modality-general representation of confidence in orbitofrontal cortex. *Cell*, 182(1):112–126.e18, July 2020. doi: 10.1016/j.cell.2020.05.022. URL <https://doi.org/10.1016/j.cell.2020.05.022>.
- [50] Loic Matthey, Irina Higgins, Demis Hassabis, and Alexander Lerchner. dsprites: Disentanglement testing sprites dataset. <https://github.com/deepmind/dsprites-dataset/>, 2017.
- [51] Kevin J. Miller, Maria Eckstein, Matthew M. Botvinick, and Zeb Kurth-Nelson. Cognitive model discovery via disentangled rnns, June 2023. URL <http://dx.doi.org/10.1101/2023.06.23.546250>.
- [52] M. L. Mittelstaedt and H. Mittelstaedt. Homing by path integration in a mammal. *Naturwissenschaften*, 67(11):566–567, November 1980. doi: 10.1007/bf00450672. URL <https://doi.org/10.1007/bf00450672>.
- [53] Manuel Molano-Mazon, Joao Barbosa, Jordi Pastor-Ciurana, Marta Fradera, RU-YUAN ZHANG, Jeremy Forest, Jorge del Pozo Lerida, Li Ji-An, Christopher J Cueva, Jaime de la Rocha, Devika Narain, and Guangyu Robert Yang. Neurogym: An open resource for developing and sharing neuroscience tasks, February 2022. URL <http://dx.doi.org/10.31234/osf.io/aqc9n>.
- [54] Milton Llera Montero, Casimir JH Ludwig, Rui Ponte Costa, Gaurav Malhotra, and Jeffrey Bowers. The role of disentanglement in generalisation. In *International Conference on Learning Representations*, 2020.
- [55] Ramon Nogueira, Chris C. Rodgers, Randy M. Bruno, and Stefano Fusi. The geometry of cortical representations of touch in rodents. *Nature Neuroscience*, 26(2):239–250, January 2023. doi: 10.1038/s41593-022-01237-9. URL <https://doi.org/10.1038/s41593-022-01237-9>.
- [56] OS Oguejiofor, AN Aniedu, HC Ejiofor, and AU Okolibe. Trilateration based localization algorithm for wireless sensor network. *International Journal of Science and Modern Engineering (IJISME)*, 1(10):2319–6386, 2013.
- [57] Maxime Oquab, Timothée Darcet, Théo Moutakanni, Huy Vo, Marc Szafraniec, Vasil Khalidov, Pierre Fernandez, Daniel Haziza, Francisco Massa, Alaaeldin El-Nouby, Mahmoud Assran, Nicolas Ballas, Wojciech Galuba, Russell Howes, Po-Yao Huang, Shang-Wen Li, Ishan Misra, Michael Rabbat, Vasu Sharma, Gabriel Synnaeve, Hu Xu, Hervé Jegou, Julien Mairal, Patrick Labatut, Armand Joulin, and Piotr Bojanowski. Dinov2: Learning robust visual features without supervision, 2023. URL <https://arxiv.org/abs/2304.07193>.
- [58] E Page. Approximations to the cumulative normal function and its inverse for use on a pocket calculator. *Journal of the Royal Statistical Society Series C: Applied Statistics*, 26(1):75–76, 1977.
- [59] Hieu Pham, Zihang Dai, Golnaz Ghiasi, Kenji Kawaguchi, Hanxiao Liu, Adams Wei Yu, Jiahui Yu, Yi-Ting Chen, Minh-Thang Luong, Yonghui Wu, Mingxing Tan, and Quoc V. Le. Combined scaling for zero-shot transfer learning, 2021. URL <https://arxiv.org/abs/2111.10050>.

- [60] Alec Radford, Jeffrey Wu, Rewon Child, David Luan, Dario Amodei, Ilya Sutskever, et al. Language models are unsupervised multitask learners. *OpenAI blog*, 1(8):9, 2019.
- [61] Mattia Rigotti, Omri Barak, Melissa R. Warden, Xiao-Jing Wang, Nathaniel D. Daw, Earl K. Miller, and Stefano Fusi. The importance of mixed selectivity in complex cognitive tasks. *Nature*, 497(7451):585–590, May 2013. doi: 10.1038/nature12160. URL <https://doi.org/10.1038/nature12160>.
- [62] Reidar Riveland and Alexandre Pouget. Generalization in sensorimotor networks configured with natural language instructions, February 2022. URL <https://doi.org/10.1101/2022.02.22.481293>.
- [63] Jonathan E. Rubin, Catalina Vich, Matthew Clapp, Kendra Noneman, and Timothy Verstynen. The credit assignment problem in cortico-basal ganglia-thalamic networks: A review, a problem and a possible solution. *European Journal of Neuroscience*, 53(7):2234–2253, May 2020. ISSN 1460-9568. doi: 10.1111/ejn.14745. URL <http://dx.doi.org/10.1111/ejn.14745>.
- [64] Ueli Rutishauser, Tyson Aflalo, Emily R. Rosario, Nader Pouratian, and Richard A. Andersen. Single-neuron representation of memory strength and recognition confidence in left human posterior parietal cortex. *Neuron*, 97(1):209–220.e3, January 2018. doi: 10.1016/j.neuron.2017.11.029. URL <https://doi.org/10.1016/j.neuron.2017.11.029>.
- [65] A. Saez, M. Rigotti, S. Ostojic, S. Fusi, and C.D. Salzman. Abstract context representations in primate amygdala and prefrontal cortex. *Neuron*, 87(4):869–881, August 2015. doi: 10.1016/j.neuron.2015.07.024. URL <https://doi.org/10.1016/j.neuron.2015.07.024>.
- [66] Rui Shu, Yining Chen, Abhishek Kumar, Stefano Ermon, and Ben Poole. Weakly supervised disentanglement with guarantees, 2019. URL <https://arxiv.org/abs/1910.09772>.
- [67] Ben Sorscher, Surya Ganguli, and Haim Sompolsky. Neural representational geometry underlies few-shot concept learning. *Proceedings of the National Academy of Sciences*, 119(43), October 2022. doi: 10.1073/pnas.2200800119. URL <https://doi.org/10.1073/pnas.2200800119>.
- [68] Ben Sorscher, Gabriel C. Mel, Samuel A. Ocko, Lisa M. Giocomo, and Surya Ganguli. A unified theory for the computational and mechanistic origins of grid cells. *Neuron*, 111(1):121–137.e13, January 2023. doi: 10.1016/j.neuron.2022.10.003. URL <https://doi.org/10.1016/j.neuron.2022.10.003>.
- [69] David Sussillo and Omri Barak. Opening the black box: Low-dimensional dynamics in high-dimensional recurrent neural networks. *Neural Computation*, 25(3):626–649, March 2013. doi: 10.1162/neco\_a\_00409. URL [https://doi.org/10.1162/neco\\_a\\_00409](https://doi.org/10.1162/neco_a_00409).
- [70] Adly Templeton, Tom Conerly, Jonathan Marcus, Jack Lindsey, Trenton Bricken, Brian Chen, Adam Pearce, Craig Citro, Emmanuel Ameisen, Andy Jones, Hoagy Cunningham, Nicholas L Turner, Callum McDougall, Monte MacDiarmid, C. Daniel Freeman, Theodore R. Sumers, Edward Rees, Joshua Batson, Adam Jermy, Shan Carter, Chris Olah, and Tom Henighan. Scaling monosemanticity: Extracting interpretable features from claude 3 sonnet. *Transformer Circuits Thread*, 2024. URL <https://transformer-circuits.pub/2024/scaling-monosemanticity/index.html>.
- [71] Loring W Tu. *Differential geometry: connections, curvature, and characteristic classes*, volume 275. Springer, 2017.
- [72] Pantelis Vafidis, David Oswald, Tiziano D’Albis, and Richard Kempter. Learning accurate path integration in ring attractor models of the head direction system. *eLife*, 11:e69841, jun 2022. ISSN 2050-084X. doi: 10.7554/eLife.69841. URL <https://doi.org/10.7554/eLife.69841>.
- [73] Xiao-Jing Wang. Synaptic reverberation underlying mnemonic persistent activity. *Trends in Neurosciences*, 24(8):455–463, August 2001. doi: 10.1016/s0166-2236(00)01868-3. URL [https://doi.org/10.1016/s0166-2236\(00\)01868-3](https://doi.org/10.1016/s0166-2236(00)01868-3).

- [74] James C. R. Whittington, Will Dorrell, Surya Ganguli, and Timothy E. J. Behrens. Disentanglement with biological constraints: A theory of functional cell types, 2022. URL <https://arxiv.org/abs/2210.01768>.
- [75] G. R. Yang and X.-J. Wang. Artificial neural networks for neuroscientists: A primer. *Neuron*, 107(6):1048–1070, September 2020. doi: 10.1016/j.neuron.2020.09.005. URL <https://doi.org/10.1016/j.neuron.2020.09.005>.
- [76] Guangyu Robert Yang, Madhura R. Joglekar, H. Francis Song, William T. Newsome, and Xiao-Jing Wang. Task representations in neural networks trained to perform many cognitive tasks. *Nature Neuroscience*, 22(2):297–306, Feb 2019. ISSN 1546-1726. doi: 10.1038/s41593-018-0310-2. URL <https://doi.org/10.1038/s41593-018-0310-2>.
- [77] Yu Zhang and Qiang Yang. An overview of multi-task learning. *National Science Review*, 5(1): 30–43, 09 2017. ISSN 2095-5138. doi: 10.1093/nsr/nwx105. URL <https://doi.org/10.1093/nsr/nwx105>.



## A Supplementary materials

### A.1 Finding fixed points of the dynamics

To find the fixed points of the network dynamics after training, we follow a standard procedure outlined in Sussillo and Barak [69]. Specifically, we keep network weights fixed, provide no inputs to the network, and instead optimize over hidden activity. Specifically, we penalize any changes in the hidden activity, motivating the network to find stable states of the dynamics in the absence of input, i.e. attractors of the dynamics. This process finds all states of accumulated evidence that can be stored in this network as short-term memory. Network dynamics could then leverage these states to maintain and update the internal representation of the ground truth  $\mathbf{x}^*$  on a single trial level, and drive downstream decisions.

### A.2 Quantification of generalization performance

To assess OOD generalization performance, we keep the trained networks fixed and train a linear decoder to predict the ground truth  $\mathbf{x}^*$  from network activity at the end of the trial. We train the decoder in 3 out of 4 quadrants and test OOD in the remaining quadrant, repeating this process 5 times for each quadrant, which results in a total of 20 OOD  $r^2$  values for each network. To account for randomness in initialization and sythetic generation of datasets, we train 5 networks for each number of tasks, resulting in a total of 100 OOD  $r^2$  values. We report the 25, 50 (median) and 75 percentiles of those values in Figure 1f,g and throughout the text. For ID generalization performance, we train on all quadrants and test in one quadrant at a time. For input dimensionality  $D > 2$ , we keep the same logic by choosing every 4-th quadrant to be sampled only in testing, repeating the process for every *mod* 4 group of quadrants.

### A.3 Derivation of theoretical $r^2$ for optimal multi-task classifiers

Here we derive the theoretical  $r^2$  for the estimation of ground truth  $\mathbf{x}^*$  from noisy data for a discrete time optimal multi-task classifier at time  $t$ .  $r^2$  is defined as:

$$r^2 = 1 - \frac{MSE(\mathbf{x}^*, \mu)}{Var(\mathbf{x}^*)} \quad (6)$$

where  $\mu$ , the mean of  $\mathbf{X}(1), \dots, \mathbf{X}(t)$ , is the prediction of the multi-task classifier (see Appendix B). The optimal estimator of  $\mathbf{x}^*$  given observations  $\mathbf{X}(1), \dots, \mathbf{X}(t)$  is denoted  $\hat{\mathbf{X}}(t) \sim \mathcal{N}(\mu(t), t^{-1}\sigma^2 I_D)$  where  $\sigma$  is the noise strength. Note that  $\mu(t) \rightarrow \mathbf{x}^*$  as  $t \rightarrow \infty$  by the central limit theorem, and  $\mu(t)$  is the optimal estimator of  $\mathbf{x}^*$  given Gaussian-noised observations. Since the dimensions in both noise and ground truth are independent, we can focus on one dimension at a time i.e.:

$$r^2 = 1 - \frac{MSE(x_i^*, \mu_i(t))}{Var(x_i^*)} = 1 - \frac{\mathbb{E}[(x_i^* - x_i^* + \mathcal{N}(0, t^{-1}\sigma^2))^2]}{Var(x_i^*)} = 1 - \frac{\sigma^2}{t Var(x_i^*)}. \quad (7)$$

Remembering that  $x_i^* \sim Uniform(-0.5, 0.5)$  it follows that  $Var(x_i^*) = \frac{2}{3}0.5^3$ , and replacing  $\sigma = 0.2$  from Table S1 we arrive to  $r^2 = 1 - \frac{0.48}{T}$  for given trial duration  $T$  which we compare to RNN OOD generalization performance in Figure S9a.

### A.4 State-space efficiency of context-dependent computation

Here we compare context-dependent decision making, where one task is performed at a time [48], to multitasking, in terms of state-space usage efficiency. Compared to the network in the main text (Figure 1c), the RNN now also receives a one-hot task rule vector indicating the current task, and it outputs the decision for that task only (Figure S1b). We have also omitted the non-linear encoder, making the tasks easier. We train the RNN for two tasks, one task at a time, in interleaved batches (Figure S1a). In one task, the RNN is required to decide which stream has more evidence, and at the other whether the sum of evidence across streams exceeds a certain decision threshold (here 0).

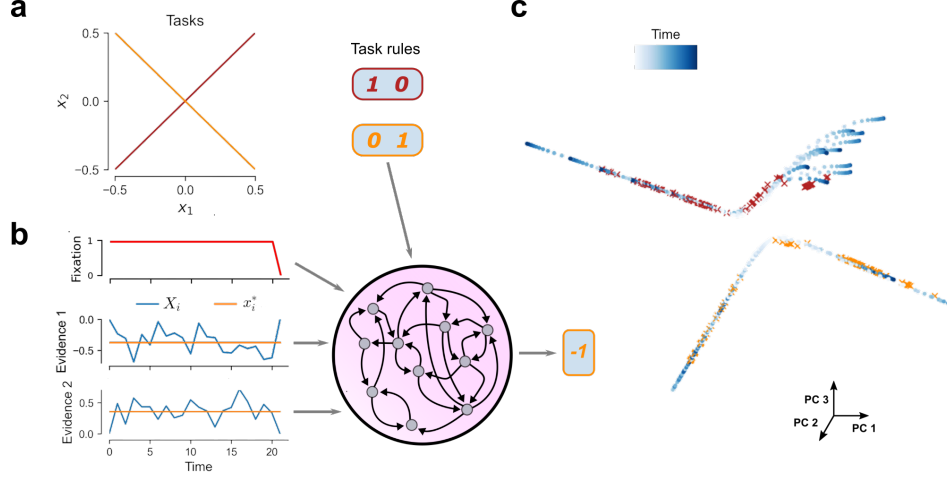


**Figure S1: Representations in an RNN trained in context-dependent decision making.** (a) We trained RNNs for two classification tasks: two-alternative forced choice (where the decision boundary is the  $x_1 = x_2$  line) and evidence integration (corresponding to the  $x_1 = -x_2$  line). Each task corresponds to a different one-hot task rule vector. (b) Network architecture. In addition to the inputs in Figure 1c, the network also a one-hot vector indicating the current task. (c), Top 3 PCs of RNN activity example trials (40 in total). The task rule biases the network towards learning separate solutions in different parts of the state space for different tasks, in the form of separate line attractors; red x's for two-alternative forced choice and orange x's for evidence integration.

We find that in this setting the network is not incentivized to learn abstract representations. Instead a separate line attractor is present in the learned dynamics for each task (red and orange x's in Figure S1c; one of the line attractors is presumably tracking the difference of evidence (similar to Yang and Wang [75] but for independent evidence streams) and the other the sum of evidence. That is to say, the task rule biases the network to learn different computations in separate regions of state space, as in Mante et al. [48]. As a result, the two dimensional latent space has collapsed and cannot be decoded from network activity; therefore generalization to any task that involves these two variables is not possible.

It follows that the network can be inefficient in terms of state space usage, because instead of compressing all of its activity around the same region, it spreads it across multiple regions, one for each task, which scales badly (linearly with the number of tasks  $N_{task}$  and exponentially with input dimensionality  $D$ ). To demonstrate the latter, imagine a family of tasks with classification boundaries of the form  $\oplus x_1 \oplus x_2 \oplus \dots \oplus x_D = 0$ , where  $\oplus \in \{+1, -1, 0\}$  is an operator indicating contribution with a positive sign, negative sign or absence of contribution for a factor to a specific task, respectively. As just shown, each one of this tasks will require its own line attractor, resulting in a total of  $3^D$  line attractors lying in separate regions of the state space, just for this simple family of tasks. As mentioned in the main text, such inefficiency can be detrimental for brains, which need to pack a lot of computation within a large yet limited neural substrate. Compare that to multitasking, which builds representations that can serve any task that involves the same latent variables, scaling linearly with  $D$ . Note that context-dependent computation can still be efficient, if tasks have a compositional structure where the solution for one task is part of the solution for another [76, 20]; in this case, representations developed for the former can act as a scaffold for representations for the latter.

## B Theoretical Derivations

Here we prove our main theoretical result outlined in Section 3.

**Notation:** lower case variables denote scalars (e.g.,  $x$ ), upper case variables denote random variables (e.g.,  $X$ ), and boldfaced variables denote vector quantities (e.g.,  $\mathbf{x}$ ,  $\mathbf{X}$ ). We denote the  $D \times D$  identity matrix as  $\mathbf{I}_D$ .

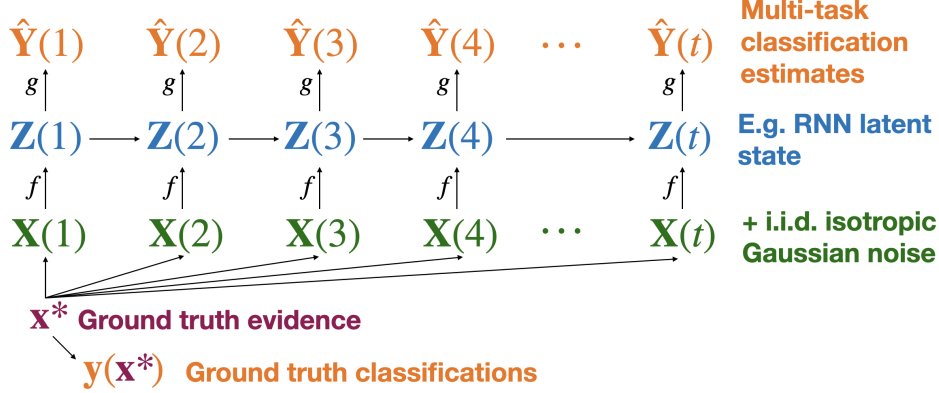


Figure S2: Bayesian graphical model framework representing our theoretical framework for multi-task classification. The agent with latent state  $\mathbf{Z}(t)$  estimates the ground truth decision output  $\mathbf{y}(\mathbf{x}^*) \in \{0, 1\}^{N_{\text{task}}}$  from noisy observations  $\mathbf{X}(t)$  transformed by injective observation map  $f$ . We prove that latent state  $\mathbf{Z}(t)$  must encode an optimal, disentangled estimate of the de-noised environment state  $\mathbf{x}^*$  when the decision boundary normal vectors  $\{\mathbf{c}_i\}_{i=1}^{N_{\text{task}}}$  span  $\mathbb{R}^D$ .

### Variable Glossary:

- $\mathbf{x}^* \in \mathbb{R}^D$  : Ground truth (un-noised) input variable of dimension  $D$ .
- $\mathbf{X}(t) \sim \mathbf{x}^* + \sigma \mathcal{N}(\mathbf{0}, \mathbf{I}_D)$  are i.i.d. noisy measurements of  $\mathbf{x}^*$ , where
  - $\sigma$  is the amount of equivariant Gaussian noise, and
  - $t$  is the discrete time index within a trial.
- $f : \mathbb{R}^D \rightarrow \mathcal{Z}$  : An injective observation map that transforms the noisy measurements  $\mathbf{X}(t)$  before they reach the latent state  $\mathbf{Z}(t)$  of the optimal estimator. The map  $f$  is injective, meaning that it preserves the uniqueness of the input, i.e., if  $f(\mathbf{x}_1) = f(\mathbf{x}_2)$ , then  $\mathbf{x}_1 = \mathbf{x}_2$ . The codomain  $\mathcal{Z}$  can be any suitable space, such as  $\mathbb{C}^M$ ,  $\mathbb{R}^\infty$ , or other spaces.
- $N_{\text{task}}$  is the number of classification tasks,
- $\{(\mathbf{c}_i, b_i)\}_{i=1}^{N_{\text{task}}}$  are the classification boundary normal vectors and offsets respectively, with  $\mathbf{c}_i \in \mathbb{R}^D$  and  $b_i \in \mathbb{R}$ . We assume each  $\|\mathbf{c}_i\| = 1$ .
- $(\mathbf{C}, \mathbf{b})$  are a matrix and vector representing each of the  $N_{\text{task}}$  classification tasks where  $\mathbf{C} \in \mathbb{R}^{N_{\text{task}} \times D}$
- $\mathbf{y}(\mathbf{x}^*) \in \{-1, +1\}^{N_{\text{task}}}$  : Ground truth classification outputs, where each ground truth classification  $y_i(\mathbf{x}^*)$  is given by

$$y_i(\mathbf{x}) = \begin{cases} +1 & \text{if } \mathbf{c}_i^\top \mathbf{x} > b_i \\ -1 & \text{otherwise} \end{cases} \quad (8)$$

- $\mathbf{Z}(t)$  : Latent variable of a multi-task classification model, conditional on  $\mathbf{X}(1), \dots, \mathbf{X}(t)$ .
- $g$  : Map from latent state  $\mathbf{Z}(t)$  to multi-task classification estimates  $\hat{\mathbf{Y}}(t)$ . For our RNN experiments, readout map  $g = \tanh$ , for instance.

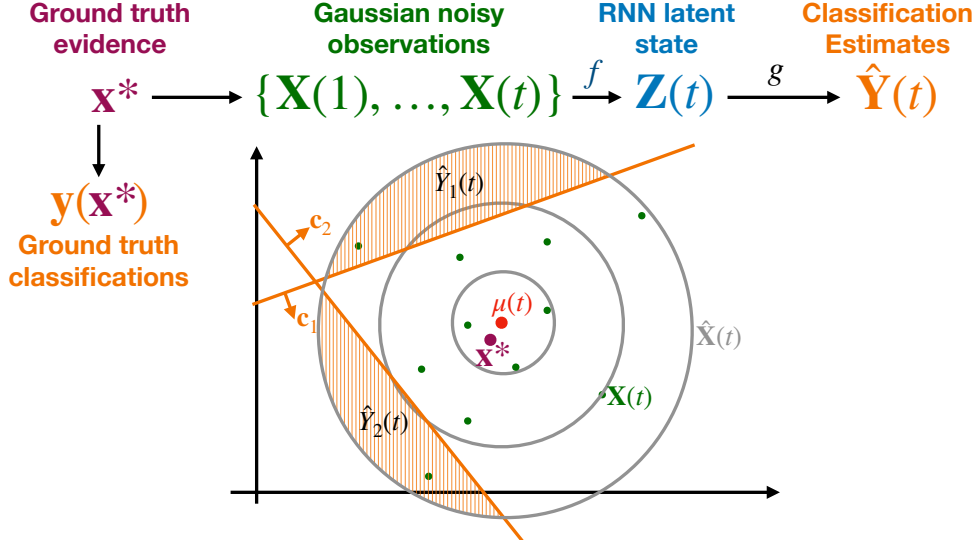


Figure S3: An overview of the classification process using an RNN with Gaussian noisy observations. The ground truth  $\mathbf{x}^*$  generates the noisy observations  $\{\mathbf{X}(1), \dots, \mathbf{X}(t)\}$ . These observations are processed by the filter-based model illustrated graphically in Figure S2, maintaining a latent state  $\mathbf{Z}(t)$ . The latent state  $\mathbf{Z}(t)$  is then used to produce classification outputs  $\hat{Y}_1(t)$  and  $\hat{Y}_2(t)$ . Theorem B.6 proves that  $\mathbf{Z}(t)$  must encode an estimate of  $\mathbf{x}^*$ , visualized in this figure, shown as  $\hat{\mathbf{X}}^*$ , including its mean  $\mu(t)$ , which is the optimal estimator for  $\mathbf{x}^*$  given the noisy observations.

- $\hat{\mathbf{Y}}(t) := g(\mathbf{Z}(t)) \in [0, 1]^{N_{task}}$  : Output vector of the multi-task classification model at time  $t$ , where each  $\hat{Y}_i(t)$  is a Bernoulli random variable estimating the conditional probability  $\Pr\{y_i(\mathbf{x}^*) = +1\}$  given the noisy observations (via latent variable  $\mathbf{Z}(t)$  – see Equation 9).
- $\hat{\mathbf{X}}(t) = \mathcal{N}(\mu(t), \Sigma(t))$  : Optimal estimate of  $\mathbf{x}^*$  given measurements  $\mathbf{X}(1), \dots, \mathbf{X}(t)$ , derived in Lemma B.1.

**Problem Statement:** We consider optimal estimators of  $\mathbf{y}(\mathbf{x}^*)$  in the multi-classification paradigm in Equation 9, shown graphically in Figure S2.

$$\mathbf{x}^* \rightarrow \mathbf{X}(1), \dots, \mathbf{X}(t) \xrightarrow{f} \mathbf{Z}(t) \xrightarrow{g} \hat{\mathbf{Y}}(t) \quad (9)$$

**Contribution:** We prove in Theorem B.6 (“Optimal Representation Theorem”) that any optimal estimator of  $\mathbf{y}(\mathbf{x}^*)$  described above will represent an optimal estimate of  $\mathbf{x}^*$  in latent state  $\mathbf{Z}(t)$ . We begin by proving results on optimal estimators in Sections B.1, B.2 with identity observation map  $f$ , developing the linear case of the optimal representation theorem (Theorem B.5) showing that the latent state  $\mathbf{Z}(t)$  must encode an estimate of  $\mathbf{x}^*$  (visualized in Figure S3). We generalize this result any injective observation map  $f$  in Section B.3 and derive closed-form solutions for extracting the estimate of  $\mathbf{x}^*$  from  $\mathbf{Z}(t)$ . We derive approximation results for  $g = \tanh$  in Corollary B.7 that show the representation of  $\mathbf{x}^*$  in  $\mathbf{Z}(t)$  will be disentangled (i.e., linear-affine decodable) if  $g = \tanh$ .

### B.1 Single Decision Boundary

First, we will derive  $\hat{Y}(t)$  for a single decision boundary with parameters  $(c, b)$ . We focus on  $P(\hat{Y}(t) | \mathbf{X}(1), \dots, \mathbf{X}(t))$ , reintroducing the latent variable  $\mathbf{Z}(t)$  later on.

Since  $y(\mathbf{x}^*)$  is a deterministic function of non-random variable  $\mathbf{x}^*$ , we will derive the probability distribution over  $P(\mathbf{x}^* | \mathbf{X}(1), \dots, \mathbf{X}(t))$  – denoted  $\hat{\mathbf{X}}(t)$  – to determine  $\hat{Y} = y(\hat{\mathbf{X}}(t))$ .<sup>1</sup>

<sup>1</sup>Note that the intermediate computation of  $\hat{\mathbf{X}}(t)$  does not imply that a system *must* compute this value to predict  $\hat{Y}$ , as the full computation of  $\hat{\mathbf{X}}(t)$  may not be necessary to determine  $\hat{Y}(t)$ .

**Lemma B.1.** Assuming no prior on  $\mathbf{x}^*$ , the conditional probability distribution  $\hat{\mathbf{X}}(t) \sim P(\mathbf{x}^* | \mathbf{X}(1), \dots, \mathbf{X}(t))$  is given by

$$\hat{\mathbf{X}}(t) = \mathcal{N}(\mu(t), \Sigma(t)) \quad (10)$$

where  $\mu(t) = \text{mean}(\mathbf{X}(1), \dots, \mathbf{X}(t))$  and  $\Sigma(t) = t^{-1}\sigma^2\mathbf{I}_D$ .

*Proof.* Since  $\mathbf{X}(1), \dots, \mathbf{X}(t)$  are i.i.d. from a Gaussian distribution with mean  $\mathbf{x}^*$  and identity covariance, the sample mean is known to be distributed normally centered at the ground truth  $\mathbf{x}^*$ . We apply the known standard deviation of the underlying distribution (identity covariance scaled by  $\sigma$ ) to arrive at  $\Sigma(t) = t^{-1}\sigma^2\mathbf{I}_D$  as the variance on the sample mean (derived from the central limit theorem).  $\square$

We can use estimator  $\hat{\mathbf{X}}(t)$  to construct  $\hat{\mathbf{Y}}(t)$  by expanding  $\hat{\mathbf{Y}}(t) = y(\hat{\mathbf{X}}(t))$  via Equation 8.

In essence, we are interested in the amount of the probability density of  $\hat{\mathbf{X}}$  that lies on each side of the decision boundary. Deriving this probability is simplified by the fact that  $\hat{\mathbf{X}}$  is isotropic – i.e., it inherits the spherical covariance of the underlying data generation process (Lemma B.2).

**Lemma B.2.**  $\hat{\mathbf{X}}(t) = \mathcal{N}(\mu(t), \Sigma(t))$  with isotropic covariance  $\Sigma(t) = t^{-1}\sigma^2\mathbf{I}_D$  and mean  $\mu(t) \in \mathbb{R}^D$ . The probability density of  $\hat{\mathbf{X}}(t)$  on the positive side of the decision boundary  $\{\mathbf{x} : \mathbf{c}^\top \mathbf{x} > b\}$  can be expressed as

$$\hat{Y}(t) \triangleq \Pr\{\mathbf{c}^\top \mathbf{x}^* > b\} = \Phi(k\sqrt{t}/\sigma) \quad (11)$$

where  $\Phi$  is the CDF of the normal distribution and  $k = \mathbf{c}^\top \mu(t) - b$  is the signed projection distance between the decision boundary and the mean  $\mu(t)$  of  $\hat{\mathbf{X}}(t)$ .

*Proof.* Since the  $\hat{\mathbf{X}}(t)$  is isotropic, the variance on every axis is equal and independent. We may rotate our coordinate system such that the projection line between the plane and the mean of  $\hat{\mathbf{X}}(t)$  aligns with an axis we denote as “axis 0”. The rest of the axes must be orthogonal to the plane. Since each component of an isotropic Gaussian is independent, the marginal distribution of  $\hat{\mathbf{X}}(t)$  on axis 0 is a univariate Gaussian with variance  $t^{-1}\sigma^2$  mean at distance  $k$  from the boundary. Equation 11 applies the normal distribution CDF  $\Phi$  to determine the probability mass on the positive side of the boundary.  $\square$

Observe that  $\hat{Y}(t)$  in Equation 11 **monotonically scales** with the signed distance  $k$  between the hyperplane and  $\mu(t)$  (CDFs are monotonic).

**Lemma B.3.** Knowledge of time  $t$  and optimal classification estimate  $\hat{Y}(t)$  is sufficient to determine the projection distance  $k$  between  $\mu(t) = \text{mean}(\mathbf{X}(1), \dots, \mathbf{X}(t))$  and the decision boundary  $(\mathbf{c}, b)$ .

*Proof.* Recall Equation 11 from Lemma B.2. We may solve for projection distance  $k$  separating the decision boundary and the mean  $\mu(t)$  of observations  $\mathbf{X}(1), \dots, \mathbf{X}(t)$  as

$$k = \frac{\sigma}{\sqrt{t}} \Phi^{-1}(\hat{Y}(t)) \quad (12)$$

Since  $\Phi$  is the CDF of the normal distribution, and the normal distribution is not zero except at  $\pm\infty$ , the inverse  $\Phi^{-1}$  is well-defined.  $\square$

## B.2 Trilateration via Multiple Decision Boundaries

**To recap Section B.1 :** We derived an optimal estimator of  $\mathbf{x}^*$  (denoted  $\hat{\mathbf{X}}(t)$ ) based on noisy i.i.d. measurements  $\mathbf{X}(1), \dots, \mathbf{X}(t) \sim \mathcal{N}(\mathbf{x}^*, \sigma^2\mathbf{I}_D)$  in Lemma B.1. In Lemma B.2 we derived the equation for Bernoulli variable  $\hat{Y}(t)$  to estimate a single classification output  $y(\mathbf{x}^*)$  based on the same noisy measurements via  $\hat{\mathbf{X}}(t)$ . Finally, we showed in Lemma B.3 that the uncertainty in  $\hat{Y}(t)$  and the time  $t$  is sufficient to determine the projection distance between the decision boundary and  $\mu(t) = \text{mean}(\mathbf{X}(1), \dots, \mathbf{X}(t))$  via Equation 12.

Let  $\hat{\mathbf{Y}}(t)$  denote the vector of classification estimates  $\hat{Y}(t)$  from Equation 12. We now have the tools to prove our final result via **trilateration**. Much like distance information from cell towers can be used to trilaterate<sup>2</sup> one's position, we will leverage Lemma B.3 and use distances from decision boundaries  $\{(\mathbf{c}_i, b_i)\}_{i \in [N_{task}]}$  to constrain the positions.

**Theorem B.4** (Trilateration Theorem). *If  $\mathbf{C}$  is full-rank, then  $\hat{\mathbf{Y}}(t)$ ,  $t$ ,  $\mathbf{b}$ , and  $\mathbf{C}$  are sufficient to reconstruct the exact value of  $\mu(t)$ , the mean of  $\mathbf{X}(1), \dots, \mathbf{X}(t)$ , which is also the optimal estimator for  $\mathbf{x}^*$ .*

*Proof.* We may prove this claim by providing an algorithm to reconstruct  $\mu(t) = \text{mean}(\mathbf{X}(1), \dots, \mathbf{X}(t))$  from  $\hat{\mathbf{Y}}(t)$ ,  $\mathbf{C}$ , and  $t$ . Invoke Lemma B.3 to compute the signed projection distance between  $\mu(t)$  and each decision plane  $(\mathbf{c}_i, b_i)$ . Let  $\mathbf{k} = [k_1, \dots, k_M]^\top$  where each  $k_i$  corresponds to decision boundary  $\mathbf{c}_i$ . Then the mean  $\mu(t)$  must satisfy

$$\mathbf{C}\mu(t) = \mathbf{k} + \mathbf{b} \quad (13)$$

Thus, for full rank  $\mathbf{C}$ , we will have a uniquely determined  $\mu(t)$  value.  $\square$

**Theorem B.5** (Optimal Representation Theorem, Linear Case). *Any system that optimally estimates  $\hat{\mathbf{Y}}$  based on noisy measurements  $\{\mathbf{X}(1), \dots, \mathbf{X}(t)\}$  must implicitly encode a representation of optimal estimator  $\mu(t) = \text{mean}(\mathbf{X}(1), \dots, \mathbf{X}(t))$  in its latent state  $\mathbf{Z}(t)$  if decision boundary matrix  $\mathbf{C}$  is full rank.*

*Proof.* This follows from the data processing inequality. We begin with the following Markov chain:

$$\mathbf{x}^* \rightarrow \{\mathbf{X}(1), \dots, \mathbf{X}(t)\} \rightarrow \mathbf{Z}(t) \rightarrow \hat{\mathbf{Y}}(t) \rightarrow \mu(t) \quad (14)$$

Put more simply, we have  $\mathbf{x}^* \rightarrow \mathbf{Z}(t) \rightarrow \mu(t)$ . Applying the data processing inequality, we obtain

$$I(\mathbf{x}^*; \mathbf{Z}(t)) \geq I(\mathbf{x}^*; \mu(t)) \quad (15)$$

where  $I(\cdot; \cdot)$  denotes the mutual information between two variables.

Since  $\hat{\mathbf{X}}(t)$  is the optimal estimator of  $\mathbf{x}^*$  given measurements  $\{\mathbf{X}(1), \dots, \mathbf{X}(t)\}$ ,  $I(\mathbf{x}^*; \mu(t)) = H(\mu(t))$ . Therefore  $I(\mathbf{x}^*; \mathbf{Z}(t)) \geq H(\mu(t))$ , implying that  $I(\mathbf{Z}(t); \mu(t)) = H(\mu(t))$ . In other words,  $\mathbf{Z}(t)$  must contain all the information of  $\mu(t)$ , and  $\mu(t)$  must be expressible as a deterministic function of  $\mathbf{Z}(t)$ .  $\square$

Theorem B.5 boils down to the observation that the confidence associated with each  $\hat{Y}_i$  in  $\hat{\mathbf{Y}}(t)$  are measures of distance between an implied estimate of  $\mathbf{x}^*$  (denoted  $\mu(t)$ ) and classification boundary  $i$  (denoted  $(\mathbf{c}_i, b)$ ).  $\hat{\mathbf{Y}}$  specifies the position of  $\hat{\mathbf{X}} = \mu$  via “coordinates” defined by decision boundary normal vectors  $\mathbf{c}_1, \dots, \mathbf{c}_{N_{task}}$ .

For sub-optimal estimators of  $\hat{\mathbf{Y}}$ , we may still obtain an understanding of the implied estimate  $\hat{\mathbf{X}}$  using the same methods. In fact, the machinery of least-squares estimation for  $\mathbf{A}\mathbf{x} = \mathbf{b}$  provides a readily accessible formula for  $\tilde{\mu}$  in sub-optimal estimators of  $\hat{\mathbf{Y}}$  (Equation 13) in the form of the Moore-Penrose pseudoinverse:

$$\tilde{\mu} = (\mathbf{C}^\top \mathbf{C})^{-1} \mathbf{C}^\top (\mathbf{k} + \mathbf{b}) \quad (16)$$

Conveniently, if the estimation errors in sub-optimal  $\hat{\mathbf{Y}}$  have a mean of zero, additional decision boundaries in  $\mathbf{C}$  (e.g., beyond the minimum  $D$  linearly independent boundaries) result in improved estimation of  $\mathbf{x}^*$  by the central limit theorem, thus generalizing our results to sub-optimal estimators.

<sup>2</sup>Trilateration differs from triangulation, and it is more frequently used in practice. Triangulation is when one has angle information w.r.t. the cell towers. Usually, this is not available – so one **trilaterates** their position [56]. This more closely matches our setting, where we just have distances information w.r.t. the decision boundaries and must determine the position.

### B.3 Optimal Representation Theorem (General Case)

We extend the results from the linear case (Theorem B.5) to the general case where observations are transformed by an injective observation map  $f$  in Theorem B.6.

**Theorem B.6** (Optimal Representation Theorem). *Let  $\mathbf{x}^* \in \mathbb{R}^D$  be a latent disentangled representation for linear binary classification task  $\mathbf{y}(\mathbf{x}^*) \in \{0, 1\}^{N_{task}}$  and  $\mathbf{X}(t) = f(\mathbf{x}^* + \sigma\mathcal{N}(\mathbf{0}, \mathbf{I}_D))$  be noisy observations transformed by an injective observation map  $f$ .*

*If  $\mathbf{C} \in N_{task} \times D$  is a full-rank matrix representing the decision boundary normal vectors in  $\mathbb{R}^D$  and  $N_{task} \geq D$ , then any optimal estimator of  $\mathbf{y}(\mathbf{x}^*)$  must encode an optimal representation of the latent variable  $\mathbf{x}^*$  in its latent state  $\mathbf{Z}(t)$ . Furthermore, the mutual information between  $\mathbf{x}^*$  and  $\mathbf{Z}(t)$  is at least as great as the entropy of the theoretically optimal estimator  $\mu(t)$ , ensuring that all the information of  $\mu(t)$  is contained in  $\mathbf{Z}(t)$ . Consequently,  $\mu(t)$  – the optimal estimate of  $\mathbf{x}^*$  based on  $f(\mathbf{X}(1)), \dots, f(\mathbf{X}(t))$  – can be written as a deterministic function (Equation 17) of latent state  $\mathbf{Z}(t)$ .*

$$\mu(t) = (\mathbf{C}^\top \mathbf{C})^{-1} \mathbf{C}^\top \left( \frac{\sigma}{\sqrt{t}} \Phi^{-1}(g(\mathbf{Z}(t))) + \mathbf{b} \right) \quad (17)$$

*Proof.* We use proof by contradiction to extend the linear case of the general representation theorem to account for injective observation maps  $f$  that map  $\mathbf{X}(t)$  before they are input to  $\mathbf{Z}(t)$ . Assume toward a contradiction that there exists a superior way of computing  $\hat{\mathbf{Y}}$  based on injectively mapped  $f(\mathbf{X}(t))$  other than learning  $f^{-1}$  and following the same procedure as when  $\mathbf{X}(t)$  was fed in directly (which we derived the optimal estimator for in Lemma B.1 and Lemma B.2). This assumption implies there is some additional information in  $f(\mathbf{X}(t))$  that is not in  $\mathbf{X}(t)$ , violating the data processing inequality.

Formally, consider the following Markov chain:

$$\mathbf{x}^* \rightarrow \{\mathbf{X}(1), \dots, \mathbf{X}(t)\} \rightarrow \mathbf{Z}(t) \rightarrow \hat{\mathbf{Y}}(t) \rightarrow \mu(t). \quad (18)$$

Since  $f$  is injective,  $f^{-1}$  exists, making  $f(\mathbf{X}(t)) \rightarrow \mathbf{X}(t)$  an equivalent transformation in terms of information content. Hence, any optimal estimator that processes  $f(\mathbf{X}(t))$  can only perform as well as if it had directly processed  $\mathbf{X}(t)$ .

Applying the data processing inequality, we have:

$$I(\mathbf{x}^*; \mathbf{Z}(t)) \geq I(\mathbf{x}^*; \mu(t)), \quad (19)$$

where  $I(\cdot; \cdot)$  denotes the mutual information between two variables. Since  $\hat{\mathbf{X}}(t)$  is the optimal estimator of  $\mathbf{x}^*$  given measurements  $\{\mathbf{X}(1), \dots, \mathbf{X}(t)\}$ ,  $I(\mathbf{x}^*; \mu(t)) = H(\mu(t))$ . Therefore,  $I(\mathbf{x}^*; \mathbf{Z}(t)) \geq H(\mu(t))$ , implying that  $I(\mathbf{Z}(t); \mu(t)) = H(\mu(t))$ . In other words,  $\mathbf{Z}(t)$  must contain all the information of  $\mu(t)$ , and  $\mu(t)$  must be expressible as a deterministic function of  $\mathbf{Z}(t)$ .

To complete the proof, we show that  $\mu(t)$  can be reconstructed from  $\mathbf{Z}(t)$ . Given the full-rank matrix  $\mathbf{C}$ , we can use the same trilateration process as in the linear case. The optimal estimate  $\mu(t)$  can be written as:

$$\mu(t) = (\mathbf{C}^\top \mathbf{C})^{-1} \mathbf{C}^\top \left( \frac{\sigma}{\sqrt{t}} \Phi^{-1}(g(\mathbf{Z}(t))) + \mathbf{b} \right), \quad (20)$$

where  $g(\mathbf{Z}(t))$  represents the transformation from the latent state to the classification probabilities. This completes the proof by showing that  $\mu(t)$  is a deterministic function of  $\mathbf{Z}(t)$ .  $\square$

Motivated by the similarity between  $\Phi(z)$  and  $\tanh(z)$ , we show that the two can be approximately canceled in Equation 17, implying that  $\mu(t)$  can be reconstructed with high accuracy with a linear-affine transformation (e.g., linear decoding) when  $g = \tanh$ . This implies that  $\mathbf{Z}(t)$  contains a linear disentangled representation of  $\mu(t)$  [30].

**Corollary B.7.** *If the readout function  $g$  is  $\tanh$ , then the reconstruction equation for  $\mu(t)$  from  $\mathbf{Z}(t)$  can be simplified using the approximation  $\Phi(z) \approx \frac{1}{2} \tanh(z) + \frac{1}{2}$ . Consequently,  $\mu(t)$  can be expressed directly in terms of  $\mathbf{Z}(t)$  without the need for the inverse CDF.*

$$\mu(t) \approx \frac{2\sqrt{3}\sigma}{\pi\sqrt{t}} (\mathbf{C}^\top \mathbf{C})^{-1} \mathbf{C}^\top \mathbf{Z}(t) + (\mathbf{C}^\top \mathbf{C})^{-1} \mathbf{C}^\top \mathbf{b} \quad (21)$$

*Proof.* Consider the readout function  $g$  given by  $g(\mathbf{Z}(t)) = \hat{\mathbf{Y}}(t) = \frac{1}{2} \tanh(\mathbf{Z}(t)) + \frac{1}{2}$ . To show that this function allows for linear decoding of  $\mathbf{x}^*$  from  $\mathbf{Z}(t)$ , we need to leverage the similarity between  $\tanh$  and  $\Phi$ .

The normal distribution CDF  $\Phi(z)$  and the function  $\frac{1}{2} \tanh(z) + \frac{1}{2}$  are known to be very similar, as both functions are sigmoid-like, centered at zero, and asymptotically approach 0 and 1 [14].

Page [58] proposed a simple approximation of  $\Phi$  via  $\tanh$ . Eliminating higher order terms, their approximation is  $\Phi(x) \approx \frac{1}{2} \tanh(\sqrt{\frac{2}{\pi}}x) + \frac{1}{2}$ . We found the following first-order approximation yielded a superior mean squared error:

$$\Phi(z) \approx \frac{1}{2} \tanh\left(\frac{\pi}{2\sqrt{3}}z\right) + \frac{1}{2}.$$

Using this approximation, we can express  $\Phi^{-1}$  in terms of  $\tanh$ :

$$\Phi^{-1}\left(\frac{1}{2} \tanh(z) + \frac{1}{2}\right) \approx \frac{2\sqrt{3}}{\pi}z.$$

Substituting this approximation into the reconstruction equation for  $\mu(t)$  from Theorem B.6:

$$\begin{aligned} \mu(t) &= (\mathbf{C}^\top \mathbf{C})^{-1} \mathbf{C}^\top \left( \frac{\sigma}{\sqrt{t}} \Phi^{-1}\left(\frac{1}{2} \tanh(\mathbf{Z}(t)) + \frac{1}{2}\right) + \mathbf{b} \right) \\ &\approx (\mathbf{C}^\top \mathbf{C})^{-1} \mathbf{C}^\top \left( \frac{\sigma}{\sqrt{t}} \left( \frac{2\sqrt{3}}{\pi} \mathbf{Z}(t) \right) + \mathbf{b} \right) \\ &= \frac{2\sqrt{3}\sigma}{\pi\sqrt{t}} (\mathbf{C}^\top \mathbf{C})^{-1} \mathbf{C}^\top \mathbf{Z}(t) + (\mathbf{C}^\top \mathbf{C})^{-1} \mathbf{C}^\top \mathbf{b}. \end{aligned}$$

Therefore, we have shown that  $\mu(t)$  can be expressed as a linear transformation of  $\mathbf{Z}(t)$  when the readout function  $g$  is  $\tanh$ . This confirms the corollary. □

## B.4 Discussion

The theoretical results presented in this appendix, particularly the Optimal Representation Theorem (Theorem B.6), provide insights into the factors driving representational convergence and alignment in neural networks and, more generally, any optimal multi-task classifier in the setup shown in Figure S2. This theorem establishes a clear connection between the latent representations learned by optimal multi-task classifiers and the true underlying data representation, offering a principled explanation for the emergence of disentangled representations aligned with the intrinsic structure of the data.

**Assumptions and Limitations:** One important consideration is the assumptions made about the noise distribution and the posterior probabilities over decision boundaries. While our main derivations assume Gaussian noise for analytical tractability, we note that the key property enabling our results is that the posterior probabilities correspond to distances from the decision boundaries in a well-behaved manner (Lemma B.3). Intuitively, this requires that the posterior distribution has a single center of mass, and integrating probability over half-spaces yields a monotonic distance function. Gaussians naturally satisfy this property as maximum entropy distributions for a given variance. Extending our results to other noise distributions satisfying similar properties is an interesting direction for future work.

**Connection to Manifold Hypothesis:** Our theoretical results have important implications for the manifold hypothesis, which posits that real-world high-dimensional data tend to lie on or near low-dimensional manifolds embedded in the high-dimensional space [23, 15]. The key insight is that our proofs show an optimal multi-task classifier must encode an estimate of the abstract coordinates of the true underlying environment state in its latent representation. Consider the abstract space in which  $\mathbf{x}^*$  resides, denoted  $\mathcal{X}^*$ . The injective observation map  $f : \mathcal{X}^* \rightarrow \mathcal{X}$ , where decision



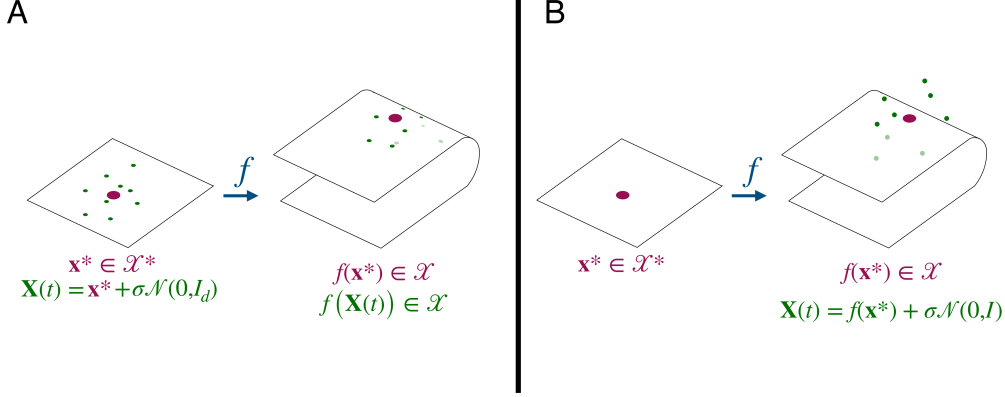


Figure S4: (A)  $\mathbf{x}^*$  is noised before being transformed by injective observation map  $f$ , resulting in observations  $f(\mathbf{X}(t))$  lying on the image of  $f$  (here  $f$  is a 2D folded surface). (b)  $\mathbf{x}^*$  is first transformed by injective observation map  $f$  and noise is added afterward, resulting in observations  $f(\mathbf{x}^*) + \sigma\mathcal{N}(0, I)$  that do not lie on the image of  $f$ .

boundaries  $y_i : \mathcal{X}^* \rightarrow \{0, 1\}$  are linear. Our results imply that an optimal classifier’s latent state  $\mathbf{Z}(t)$  must encode abstract coordinates in  $\mathcal{X}^*$  rather than ambient coordinates  $\mathcal{X}$ .

The injective observation map  $f$  aligns closely to the typical conception of a data manifold (e.g., if  $f \in C^1$  or  $f \in C^n$ , as described in [71]). The abstract space  $\mathcal{X}^*$  can be seen as the intrinsic coordinate system of the manifold, while  $f$  maps these coordinates to the high-dimensional observation space  $\mathcal{X}$ . Our findings suggest that an optimal classifier will implicitly learn to invert this mapping to recover the abstract coordinates. Moreover, for natural data where the manifold hypothesis holds, the learned latent representation would plausibly capture the manifold structure, as this is essential for disambiguating noisy observations and estimating the true underlying state. The low-dimensional manifold structure is a key prior that an optimal classifier can (and in our case must) exploit to improve its performance.

**Ordering of Noise and Observation Map:** The ordering of the noise and the non-linear observation map matters for the latent space representation. When the noise is applied before the observation map, the noisy observations are constrained to lie on a manifold with the same intrinsic dimension as the true latent space  $\mathcal{X}^*$ . In contrast, when the noise is applied after the observation map, the noisy observations can deviate from the low-dimensional manifold, potentially introducing degeneracy where two noised observations arising from different  $\mathbf{x}^*$  may appear identical (i.e., non-injective). Imagine  $\mathcal{X}^*$  as a 2D piece of paper. An injective, smooth, continuous observation map  $f : \mathcal{X}^* \rightarrow \mathcal{X}$  where  $\mathcal{X}$  is a 3-dimensional space “crumples” the sheet of paper  $\mathcal{X}^*$  into a crumpled ball in  $\mathcal{X}$ . If you add noise after the mapping, a point on one corner of the paper could get “popped out” of the 2D manifold by the noise and end up very far away on the crumpled surface if you were to examine it flattened out (illustrated in Figure S4).

The curvature of the observation map  $f$  and the level of noise  $\sigma$  are fundamental factors influencing the extent of the degeneracy introduced by the noise after the observation map. High curvature in  $f$  can make the intrinsic geometry of the data more challenging to identify (e.g., more tightly crumpled paper). Large noise levels can push observations further from the underlying manifold, similarly worsening the potential degeneracy in the observations. Interestingly, this degeneracy is a key concern in work on visual predictive coding for map learning by Gornet and Thomson [26]. They demonstrate that a predictive coding network can learn to map a Minecraft environment with visually degenerate states by integrating information to perform predictive coding along trajectories within the environment.

**Connection to the Platonic Representation Hypothesis:** Our results provide a new perspective on the Platonic representation hypothesis [34]. The Platonic representation hypothesis suggests that the convergence in deep neural network representations is driven by a shared statistical model of reality, like Plato’s concept of an ideal reality. Convergence of representations is analyzed in terms of

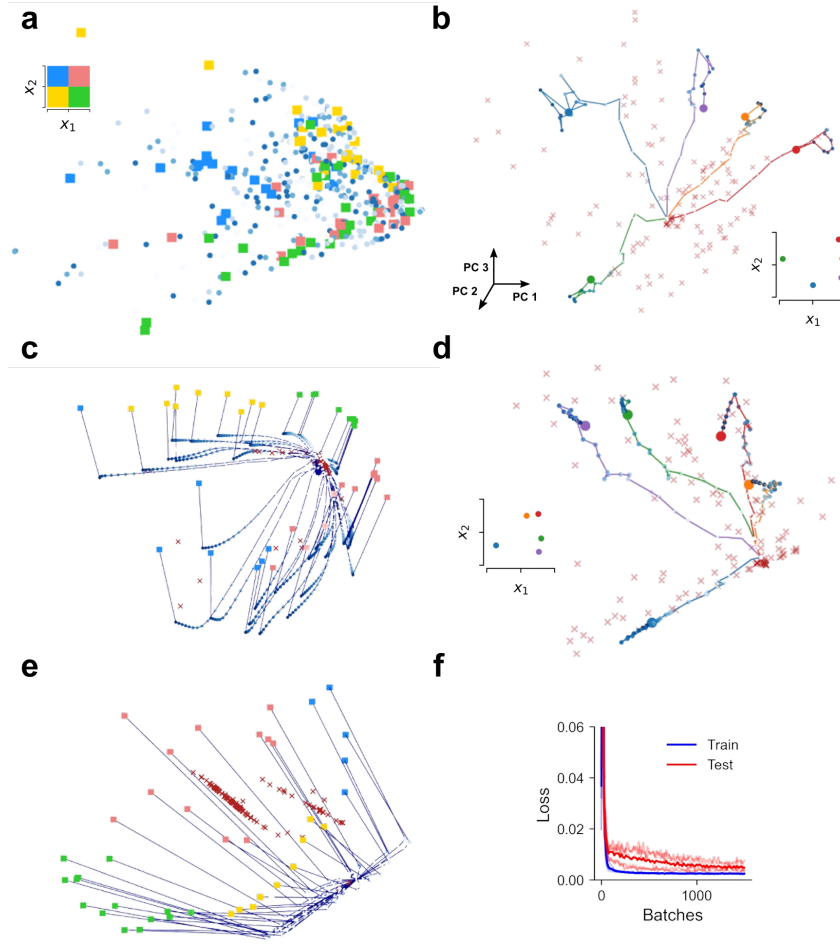
similarity of distances between embedded datapoints among AI models trained on various modalities. While the authors of the hypothesis argue that energy constraints might lead to divergence from a shared representation for specialized tasks, our Optimal Representation Theorem suggests that the key factor driving convergence is the diversity and comprehensiveness of the tasks being learned. As long as the tasks collectively span the space of the underlying data representation, convergence to a shared, reality-aligned representation can occur, even in the presence of energy or computational limitations. Our theoretical results amount to a necessary condition for optimal multi-task classifiers to represent a disentangled representation of the data within their latent state. With energy constraints, extraneous network activity may be regularized out of the model, resulting in greater alignment between disentangled representations in energy constrained models that “understand” the Platonic nature of reality. The very energy constraints [34] suggest may lead to divergence could actually facilitate convergence of the platonic representations, as they may encourage the learning of simple, generalizable features that capture the essential structure of the data. This insight opens up interesting avenues for future research on the interplay between task diversity, energy constraints, and the emergence of shared representations. Finally, energy constraints have been shown to naturally lead to predictive coding [1], tightening the relationship between energy efficiency, prediction, and cognitive map learning.

**Implications and Future Directions:** The theoretical analysis presented in this appendix sheds light on the factors driving the emergence of disentangled representations in neural networks and their alignment with the intrinsic structure of the data. By formalizing the conditions under which learned representations recover the true underlying data manifold, our work provides a foundation for understanding the remarkable success of representation learning across diverse domains. Avenues for future research include extending our results to more general noise distributions, exploring the sample complexity of learning under different observation maps and noise levels, and empirically validating the convergence of representations across models and modalities in the context of task diversity and energy constraints.

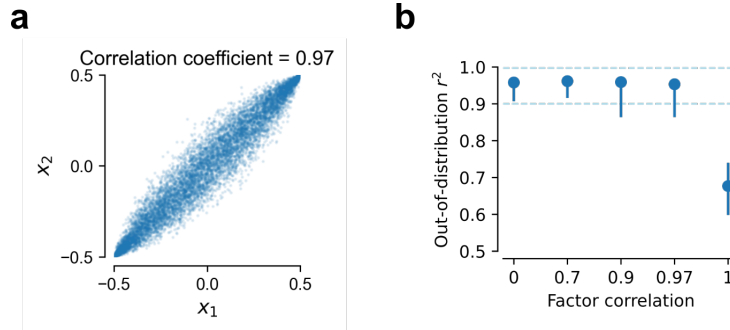
## C Supplementary figures

Table S1: **Hyperparameter values for RNN training.** These values apply to all simulations, unless otherwise stated.  $\tau = 100ms$  was chosen as a conservative estimate of membrane time constant.  $\sigma$  was varied in simulations (e.g. Figure 3b). We found that free RT tasks benefited from a higher learning rate. Other hyperparameters worked out of the box.

PARAMETER	VALUE	EXPLANATION
$\Delta t$	100 MS	EULER INTEGRATION STEP SIZE
$\tau$	100 MS	NEURONAL TIME CONSTANT
$N_{neu}$	64	NUMBER OF HIDDEN NEURONS
$\sigma$	0.2	INPUT NOISE STANDARD DEVIATION
$T$	20	TRIAL DURATION (IN $\Delta t$ s)
$\eta_0$	0.001/0.003	ADAM LEARNING RATE FIXED/FREE RT
$B$	16	BATCH SIZE
$N_{batch}$	$10^5$	NUMBER OF TRAINING BATCHES
$D$	2	DIMENSIONALITY OF LATENT SPACE



**Figure S5: Details of learned representations and of learning.** (a) Representation after the decoder. 3 out of 40 features were chosen randomly to be displayed. Compared to Figure 1d the representations wrap around non-linearly, and the quadrants are overlapping. The RNN needs to invert the non-linear mapping and remove the noise to arrive at disentangled representations. (b) Individual trial examples from network in Figure 1c. Plotting conventions same as in Figure 1d, except here every trial has been mapped to a separate color (lines and final dot). The ground truth  $\mathbf{x}^*$  for these example trials is shown in the bottom right, and the attractors have been made transparent for better visibility. Note that these trials include noise, like the ones the network has been trained on. As can be seen, the network maintains a sense of metric distances in the 2D space: examples close in state space are also close in representation space. (c) Representation early in learning, for a network trained with 1/4 of the examples compared to Figure 1d. The representation is not abstract yet, however it is visible how the quadrants start separating and the attractors start spreading in the 2D manifold. (d) Same as in (b), but for network with a delay period of 500 ms (5 darker dots at the end of trajectories). Activity remains localized after the removal of the evidence streams, maintaining a short-term memory of the joint evidence with only minor leaks. (e) Representation learned in a network trained without input noise ( $\sigma = 0$ ). Trajectories separate from the beginning, and there is no pressure to learn a 2D continuous attractor anymore. (f) Train and test errors for linear decoder for the OOD generalization task. Transparent lines correspond to different quadrants while opaque lines to the average across quadrants for one network.



**Figure S6: Disentanglement and factor correlations.** (a) We introduce strong correlations in the latent factors, rendering parts of the state space virtually invisible to the network during pre-training (trained for a total of 24 classification tasks). (b) Despite that, generalization performance is excellent for correlations very close to 1. Once the factors are perfectly, performance drops significantly. This implies that the network can learn a disentangled representation from correlated inputs, as long as there is some signal about the factors independently. This finding goes beyond [38] to show that the multi-task learning setting allows OOD generalization when the distribution during training the RNN itself is vastly different than the one during testing.

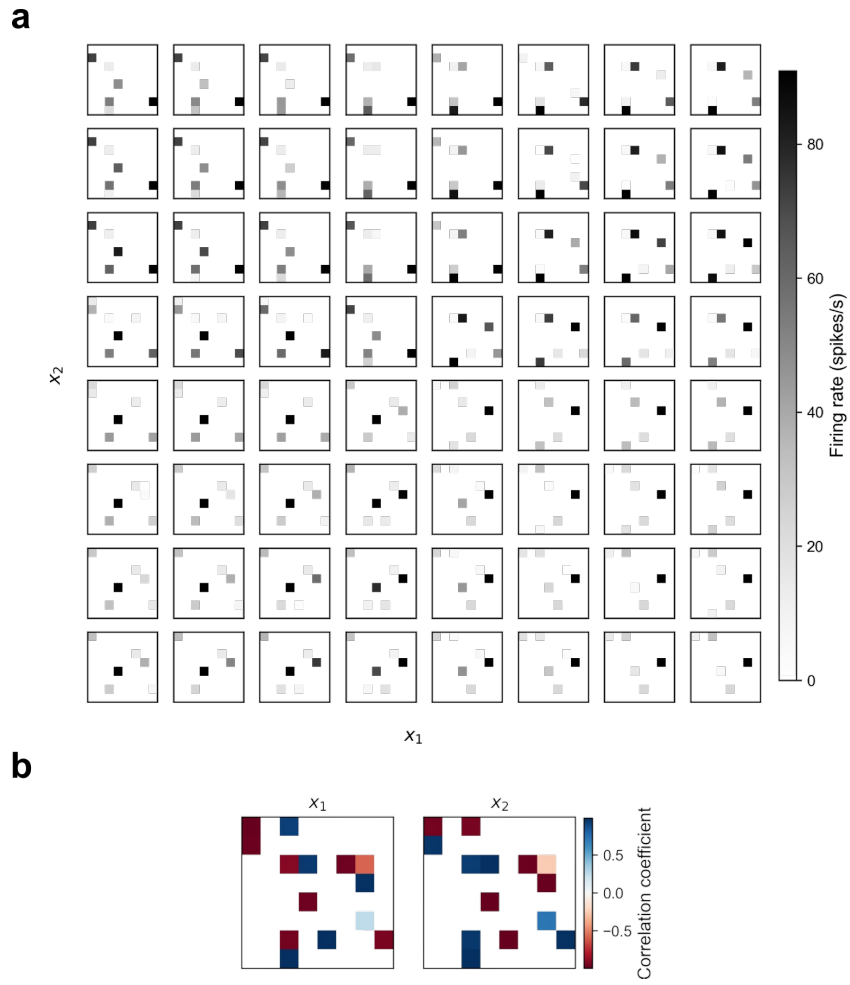


**Figure S7: RNN activations and relation to latent variables. (a)** Steady-state firing rates of hidden layer of RNN in Figure 1c, while systematically varying  $x_1$  and  $x_2$  from -0.5 to 0.5. Firing rates for a total of 64 neurons are plotted in 8\*8 grids, one for each value of  $x_1$  and  $x_2$ . **(b)** Correlation coefficient of steady-state firing rates with  $x_1$  and  $x_2$ , respectively.

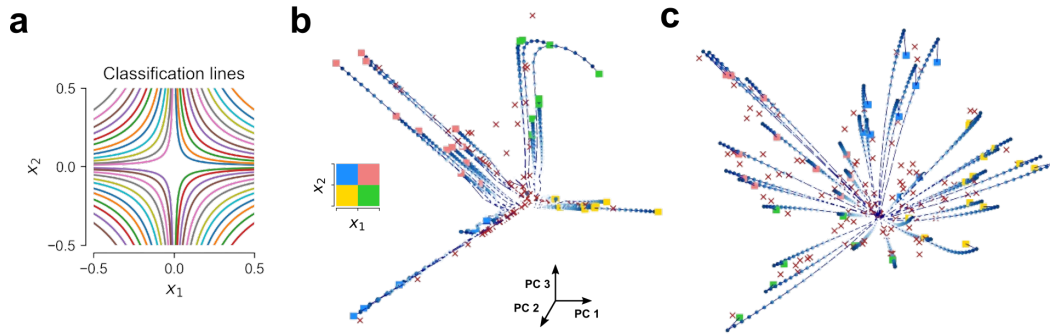


**Figure S8: Representations for a multiplicative task and for continual learning.** (a) Classification lines for the multiplicative task. There is a total of 48 classification lines, 12 per quadrant. (b) Top 3 PCs of RNN activity over trials. The network still learns a two-dimensional continuous attractor, however the trajectories of different quadrants separate. (c) The network learns an abstract representation when trained for the linear and multiplicative tasks in interleaved batches, and unlike in b the trajectories of different quadrants do not separate.

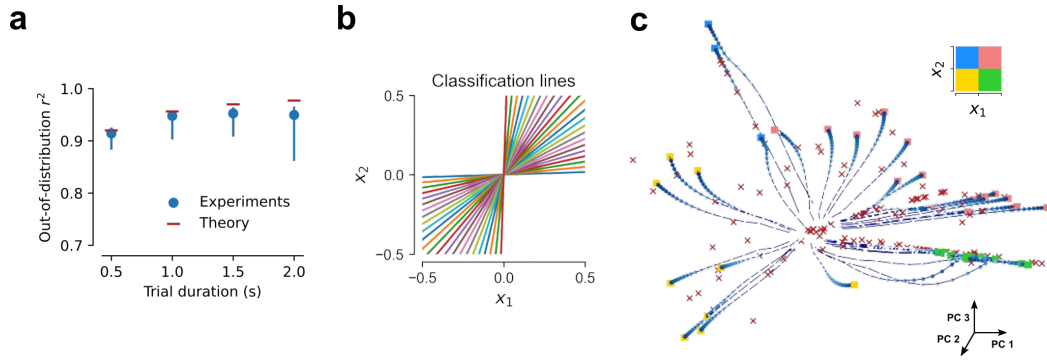


**Figure S9: RNN simulations confirm and extend theoretical predictions.** (a) OOD  $r^2$  for free RT network required to report its estimate of  $\mathbf{x}^*$  at different times. Maximum network  $r^2$  matches optimal multi-task classifier theory predictions (Equation (7)). (b) We now let task demands cover only half the state space, i.e. let the 24 classification lines only cover quadrants 1 and 3. (c) Top 3 PCs of RNN activity over trials for network trained in classification lines that cover half of the state space. The network still learns a two-dimensional continuous attractor, however the representation now is not disentangled, compared to Figure 1d. For example notice how the representation of the blue and green quadrants has collapsed in the absence of task demands, and how the yellow quadrant lies on a different 2D plane than the red.